Master Thesis No. 3771
cand. M. Sc. Maike Ostermann

Model Predictive Control and Moving Horizon Estimation for Solar Tower Power Plants: Analysis and Adaptations to the Experimental Facility Solar Tower Jülich

Modellprädiktive Regelung und Moving-Horizon-Schätzung für Solarturmkraftwerke: Analyse und Anpassungen an das Forschungskraftwerk Jülich

Date of issue:	15.05.2023
Date of submission:	15.12.2023
Supervising tutors:	M.Sc. David Zanger (DLR) M.Sc. Johannes Lips (IFK)
Examiner:	Univ.-Prof. Dr.-Ing. Hendrik Lens

Submitted to the University of Stuttgart

University of Stuttgart
Institute of Combustion and
Power Plant Technology (IFK)

Eigenständigkeitserklärung

Ich versichere, dass die bereitgestellte elektronische Fassung der studentischen Arbeit mit der von der Universität Stuttgart nach Maßgabe der einschlägigen Prüfungsordnung angenommenen bzw. bewerteten Originalfassung der studentischen Arbeit in Form und Inhalt übereinstimmt.

Ich erkläre, dass ich die Arbeit selbständig verfasst und bei der Erstellung die einschlägigen Bestimmungen, insbesondere zum Urheberrechtsschutz fremder Beiträge, eingehalten habe. Soweit meine Arbeit fremde Beiträge (z.B. Bilder, Zeichnungen, Textpassagen) enthält, erkläre ich, dass diese Beiträge als solche gekennzeichnet sind (z.B. Zitat, Quellenangabe) und ich eventuell erforderlich gewordene Zustimmungen der Urheber zur Nutzung dieser Beiträge in meiner Arbeit eingeholt habe. Für den Fall der Verletzung Rechter Dritter durch meine Arbeit erkläre ich mich bereit, der Universität Stuttgart einen daraus entstehenden Schaden zu ersetzen bzw. die Universität Stuttgart auf deren Aufforderung von eventuellen Ansprüchen Dritter freizustellen. Weiterhin erkläre ich, dass diese Arbeit weder vollständig noch in wesentlichen Teilen Gegenstand eines anderen Prüfungsverfahrens gewesen ist und dass ich die Arbeit weder vollständig noch in Teilen bereits veröffentlicht habe.

Ich erkenne die Aufgabenstellung an und beachte das "Merkblatt zur Durchführung und Anfertigung von studentischen Arbeiten am IFK" in der aktuellen Fassung.

Ort, Datum, Unterschrift

Universität Stuttgart
Institut für Feuerungs- und
Kraftwerkstechnik

Pfaffenwaldring 23 • 70569 Stuttgart • T +49 (0) 711 685-63487 • F +49 (0) 711 685-63491 • ifk@ifk.uni-stuttgart.de

Stuttgart, 12.05.2023

Masterarbeit Nr. 3771
für Frau cand. M.Sc. TechKyb *Maike Ostermann*
Matr.-Nr. 3539468

Experimentelle Validierung einer modellprädiktiven Regelung am Solarturm Jülich

Experimental Validation of a Model Predictive Controller at the Solar Tower Jülich

1. Problembeschreibung

Um den Ausbau von Solarturmkraftwerken wirtschaftlich attraktiver zu machen, ist eine Steigerung des Wirkungsgrads von großer Bedeutung. Hierbei muss jedoch insbesondere ein sicherer Betrieb gewährleistet sein. Eine besonders schwierig zu beherrschende Störgröße sind Wolkendurchzüge, die einen Teil des Heliostatenfeldes verschatten. Während der Wolkendurchzüge sinkt die eingestrahlte Leistung auf dem Receiver und die Ausgangstemperatur des Wärmeübertragungsmediums verringert sich. Eine Verringerung der Austrittstemperatur ist jedoch zu vermeiden, da dies die Effizienz des Kraftwerks herabsenkt und die Lebensdauer reduziert. Das Abfallen der Temperatur kann jedoch durch zwei Stellgrößen beeinflusst werden. Zum einen durch den Massenstrom des Wärmeübertragungsmediums und zum anderen durch das Erhöhen der eingestrahlten Leistung. Die eingestrahlte Leistung kann dabei durch Verschieben der Zielpunkte der Heliostaten geändert werden. In der Literatur werden die Regelung des Massenstroms und der Zielpunkte meist getrennt behandelt. Dies ermöglicht jedoch keine optimale Regelung der Ausgangstemperatur unter Einhaltung der Temperaturgrenzen.

2. Zielsetzung

Ziel der Arbeit ist es eine modellprädiktive Regelung für den Solarturm Jülich auszulegen und zu validieren. Die Regelung soll sowohl Massenstrom und Zielpunkte regeln unter Berücksichtigung der Wolkenvorhersage. Die Regelung soll dabei die Exergie der Luft (Wärmeübertragungsmedium) maximal halten ohne die Temperaturbegrenzungen der Receiveroberfläche zu überschreiten. Die Funktionsweise und Grenzen der Regelung sollen durch unterschiedliche fiktive Wolkenszenarien am Solarturm validiert werden.

3. Durchzuführende Arbeiten

- Einarbeitung in das Themengebiet der modellprädiktiven Regelung (MPR), der Zielpunktregelung und der Thermodynamik keramischer Receiver (2 Wochen)
- Einarbeitung in den bestehenden Programmcode (2 Wochen)
- Anpassen der bestehenden MPR an die Anforderungen des realen Solarturms (die bestehende MPR wurde bereits weitestgehend für den Solarturm Jülich ausgelegt, es sind jedoch für den realen Betrieb noch ein paar Anpassungen notwendig) (2 Wochen)
- Auslegen eines Beobachters für die Regelung (2 Wochen)
- Entwurf eines Wolkensimulationssystems am Solarturm Jülich durch Fokussieren und Defokussieren der Heliostaten (2 Wochen)
- Anbinden der Regelung an bestehende Sensorik und Aktorik am Solarturm Jülich (2 Wochen)
- Experimente für unterschiedliche Wolkenszenarien durchführen. (2 Wochen)
- Auswerten der Experimente (2 Wochen)
- Verfassen einer Abschlussarbeit (8 Wochen)

Die studentische Arbeit wird beim *Deutschen Zentrum für Luft- und Raumfahrt, Institut für Solarforschung* durchgeführt und dort von Herrn *David Zanger* betreut. Die Betreuung am IFK erfolgt durch Herrn *Johannes Lips.*
Das Merkblatt zur Durchführung und Anfertigung von studentischen Arbeiten am IFK ist zu beachten, ebenso die „Richtlinie für die Abwicklung von studentischen Arbeiten in den Studiengängen der Gemeinsamen Kommission Maschinenbau der Fakultäten 4 und 7“. Über den Fortgang der Arbeit ist in regelmäßigen Abständen (alle 4 - 6 Wochen) am IFK zu berichten.

Beginn der Arbeit: *15.05.2023*
Abgabetermin: *15.11.2023*

LIPS

(*Prof. Dr.-Ing. Hendrik Lens*)

(*Johannes Lips*)

Abstract

This thesis presents the extension of a model predictive control design by a moving horizon estimator, applied at the experimental facility Solar Tower Jülich.

The control addresses challenges posed by cloud passages, aiming to maximize the receiver outlet power and maintain a stable outlet temperature despite solar radiation fluctuations. A safe operation has to be ensured by preventing overheating and thermal stresses in the receiver caused by fast temperature changes. These occur when the solar radiation increases rapidly after a cloud passage. The control adjusts the heat transfer fluid's mass flow and the heliostat aim points, incorporating cloud predictions to proactively handle solar radiation changes.

The moving horizon estimator adapts the receiver model's parameters, attempting to improve the model accuracy and thus, enhance the efficiency and robustness of the control. The control performance was tested in simulation for different cloud coverages. By applying inaccurate cloud prediction, the robustness of the control was evaluated, yielding improvements of up to 60 % compared to the control without the parameter estimation.

Tests conducted at the Solar Tower Jülich revealed shortcomings in the control design. The applied receiver model showed insufficient accuracy even when applying the parameter estimation. The real-time capability of the control was not ensured due to long delay times of the heliostats and increased process times. The thesis suggests to adapt and validate the receiver model and to enhance the real-time capability through improvements in the computational performance and the heliostat field operating system.

Kurzfassung

Die vorliegende Arbeit erweitert einen modellprädiktiven Regelungsansatz am Solarturmkraftwerk Jülich um einen Moving-Horizon-Schätzer.

Die Regelung hat zum Ziel, die Receiverleistung zu maximieren und die Ausgangstemperatur konstant zu halten, insbesondere bei Wolkendurchzügen. Schnelle Temperaturanstiege, die durch einen Änderungen der solaren Einstrahlung nach einer Wolkenpassage entstehen können, müssen vermieden werden, um eine Überhitzung des Receivers und thermische Spannungen zu vermeiden. Die Stellgrößen der Regelung sind der Massenstrom des Wärmeübertragungsmediums und die Zielpunkte der Heliostaten. Um bevorstehende Schwankungen in der solaren Einstrahlung zu antizipieren, bezieht die Regelung Wolkenvorhersagen ein.

Der Schätzer optimiert die Modellparameter des Receivers, um das Modell und damit die Regelgüte für unterschiedliche Wolkenszenarien zu verbessern. Simulationen mit ungenauen Wolkenvorhersagen testen die Robustheit der Regelung und zeigen eine Verbesserung von bis zu 60 % gegenüber der Regelung ohne Parameterschätzung.

Tests am Solarturm Jülich zeigen Defizite der Regelung auf, darunter die unzureichende Genauigkeit des Receivermodells und lange Verzögerungszeiten der Heliostaten. Weitere Messungen und eine Verbesserung des Receivermodells und der Echtzeitfähigkeit der Regelung werden empfohlen.

Table of Contents

List of Figures

List of Tables

List of Symbols

Greek symbols

Symbol	Description
κ_1, κ_1	Aim point control inputs
μ_{bounds}	Design factor for parameter bounds
$\mu_{\dot{m}}$	Mass flow ratio
ξ	Slack variable for soft constraints

Latin Symbols

Symbol	Description
d	Orifice diameter of absorber cup
D	Damping constant for fan model
F_{solar}	Solar flux density
h_{amb}	Specific enthalpy of ambient air
$\dot{H}_{\text{amb}}$	Enthalpy flow of ambient air
$h_{\text{inlet},x}$	Specific enthalpy of air at position x
$\dot{H}_{\text{inlet},x}$	Enthalpy flow of air at position x
h_{out}	Specific enthalpy of outlet air
$\dot{H}_{\text{out}}$	Enthalpy flow of outlet air
h_{sector}	Specific enthalpy of a header sector
$\dot{H}_{\text{sector}}$	Enthalpy flow of a header sector
J	Objective function of MPC optimization problem
K_p	Proportional gain of fan model
L	Stage cost of MPC objective function
$\dot{m}_{\text{abs}}$	Air mass flow through an absorber cup
$\dot{m}_{\text{rec}}$	Air mass flow through the entire receiver
$\dot{m}_{rec,red}$	Reduced air mass flow through the representative cups
$\dot{m}_{\text{setpoint}}$	Set point value of the fan/valve combination
M	Terminal cost of MPC objective function
$n_{\text{heliostats}}$	Amount of heliostats in the heliostat field

Symbol	Description
$n_{\text{heliostats,focused}}$	Amount of heliostats focused on the receiver
N	Prediction horizon
$\mathbf{p}$	Model parameters
$\mathbf{P_p}$	Weighting matrix for model parameters in MHE objective
$\mathbf{P_v}$	Weighting matrix for process noise in MHE objective
$\mathbf{P_w}$	Weighting matrix for measurement noise in MHE objective
$\mathbf{P_x}$	Weighting matrix for states in MHE objective
$\dot{Q}_{\text{loss,header}}$	Heat loss of a header
$\mathbf{r}$	Reference trajectory
$\mathbf{R}$	Weighting matrix for input penalty in MPC objective
T	Time constant for fan model element
$T_{\text{abs,back}}$	Temperature of the backside of the absorber comb
$T_{\text{abs,front}}$	Temperature of the front of the absorber comb
$T_{\text{abs,front},SS}$	Steady-state temperature of the front of the absorber comb
$T_{\text{inlet},x}$	Temperature of the air at position x
$T_{\text{inlet},x,SS}$	Steady-state temperature of the air at position x
t_n	Current time
$T_{\text{return},3}$	Temperature of the return air
t_{step}	Sampling time
$\mathbf{u}$	Control inputs variables
$\mathbf{u}_{\text{lb}}, \mathbf{u}_{\text{ub}}$	Lower and upper bounds of control inputs
$\mathbf{v}$	Measurement noise
$\mathbf{w}$	Process noise
w_1, w_2	Weighting matrices for MPC objective terms
$\boldsymbol{w_\xi}$	Weighting matrix for the soft constraints in MPC objective
$\mathbf{x}$	System states
$\mathbf{x}_{\text{lb}}, \mathbf{x}_{\text{ub}}$	Lower and upper bounds of states
$\mathbf{y}$	Output variables
$\mathbf{z}$	Algebraic variables

List of Abbreviations

CSP	Concentrated Solar Power
DAPS	Dynamic Aimpoint Processing System
DLR	German Aerospace Center (Deutsches Zentrum für Luft- und Raumfahrt)
DNI	Direct Normal Irradiance
EKF	Extended Kalman Filter
HTF	heat transfer fluid
MHE	Moving Horizon Estimator
MPC	Model Predictive Control
OPC	Open Platform Communications
RMSE	Root Mean Square Error
UKF	Unscented Kalman Filter

1 Introduction

1.1 Motivation

In recent years, the focus on sustainable energy solutions has intensified. The global warming caused by excessive greenhouse gas emissions has led to increasing efforts to raise the share of renewable energy sources. International treaties like the Paris Agreement from 2015 have set the goal to limit the global warming to 1.5 °C above pre-industrial levels (United Nations, 2015).

To achieve this goal, several renewable energy sources have to be combined to build a sustainable and reliable energy system. In the field of solar energy technologies, Concentrated Solar Power (CSP) systems are gaining increasing interest. Currently about 6.3 GW of CSP systems are installed worldwide (REN21, 2023). They use reflective surfaces to concentrate solar radiation onto a receiver, where the energy is transferred to a heat transfer medium. The heat is used to power a steam turbine for electricity generation or utilized in other applications.

Due to the power generation with steam turbines, CSP systems can provide similar grid stability services as conventional power plants, contributing to the stability of the electrical grid. Furthermore, most commercial CSP systems are combined with thermal storage tanks. These enable a more flexible operation, as the power generation is detached from the availability of the primary energy source. This is an important advantage over photovoltaic, or wind systems. Consequently, CSP systems can help to address the challenges associated with the transition towards an energy system based on renewable energy sources.

CSP systems include parabolic trough, linear Fresnel, parabolic dish, and solar tower systems, which differ in the way they track the sun and concentrate the solar radiation (Boretti et al., 2019). Compared to linear focusing systems (linear fresnel, parabolic trough), point focus systems like the solar tower or parabolic dish can achieve much higher concentration factors, leading to higher temperatures and thus increased process efficiencies (Belhomme, 2011)(Zhang et al., 2013).

Even though parabolic trough systems are currently the most prevalent CSP technologies, solar tower systems are gaining increasing interest, due to their good scale-up potential. Based on the data provided by Thonig et al. (2023), 27 solar tower power plants were operational in 2023, yielding a total capacity of 1.46 GW. In China, the currently fastest growing market in CSP systems, 63 % of projects are planned to use solar tower systems (REN21, 2023). Some of the commercial solar tower plants are designed as hybrid systems, combining the central receiver with other technologies like parabolic trough, photovoltaic or wind systems, making the plants more cost-effective (REN21, 2023).

To further enhance the economic viability of solar tower power plants, it is crucial to improve their efficiency even more. This is particularly significant for large scale projects.

Research on different aspects of solar tower power plants is ongoing, for example concerning the used heat transfer mediums or the receiver types. Another way to increase the efficiency is the optimization of the applied control strategies. The operational challenges faced by solar power tower plants include fluctuations in the solar irradiance caused by varying cloud conditions. These disturbances decrease the efficiency or, in more severe cases, can cause critical damage to the receiver.

Some research has been done on the control of cloud disturbances but the majority of these studies focus on the control of the solar flux density distribution on the receiver without controlling the mass flow of the heat transfer fluid. With the increase of computational power in recent years, advanced control strategies like model predictive control are taken into consideration for the control of solar tower plants. In combination with cloud prediction systems, they present a promising way to mitigate the impact of cloud disturbances and thus, increase the efficiency of the plants. However, only a very limited number of approaches using this control design have been proposed in the past and even fewer have been tested on real plants.

1.2 Objective

The objective of this thesis is the adaption and evaluation of an advanced control design, optimizing the operation of the solar tower power plant in Jülich. It is based on a previously developed model predictive controller by Geschonneck (2023).

The control aims to address the challenges associated with dynamic environmental conditions, specifically cloud coverages. A particular challenge of the control during cloud disturbances is the sudden rise in the solar power projected on the receiver when the cloud passes. Insufficient control interventions can evoke exceeding surface temperatures or rapid temperature changes, causing thermal stresses in the receiver. Thus, the controller incorporates cloud predictions to anticipate the cloud passage by adjusting the control inputs in advance. The goal is to maintain the receiver outlet temperature to a set point value and maximize the energy output while always ensuring a safe operation.

In contrast to most other control designs, the approach combines the control of the power projected on the receiver with the control of the mass flow of the heat transfer fluid.

The existing model predictive control design will be complemented by a moving horizon estimator. The estimator is supposed to enhance the accuracy of the used receiver model by adapting the model parameters. Furthermore, additions to the objective function of the control will be applied. In order to evaluate the performance and robustness of the new control setup, it will be tested in simulation and on the real plant regarding different cloud scenarios and cloud prediction accuracies. The results should provide insights into the performance of the controller and estimator and their potential to improve the efficiency and robustness of the solar tower power plant in Jülich.

1.3 Structure

The thesis is sectioned into seven chapters, beginning with the fundamentals of solar tower power plants and the specifications of the Solar Tower Jülich. Additionally, the chapter introduces underlying control theory, including the definitions for the model predictive control and moving horizon estimation algorithms. The toolbox employed in the implementation is presented, and a review of existing literature on the control of solar tower power plants is provided.

Following the fundamentals chapter, the used models of the solar tower subsystems will be described. They are based on the models applied in Geschonneck (2023) and adapted by Zanger (2023).

Afterwards, the complete control setup will be presented, including the adaptions on the model predictive controller, the design of the moving horizon estimator, and their integration into the solar tower environment in Jülich. Since the design choices are closely connected to the performance of the combined control system, an analysis of the heliostat movement times and the computation times of the control loop is included in this chapter as well.

The simulation results are presented in Chapter 5. They incorporate different cloud scenarios and cloud prediction accuracies to assess the performance and robustness of the control. It will be investigated, if the moving horizon estimator can improve the performance of the controller by adapting the receiver model parameters.

Following the simulations, Chapter 6 contains the results of the experiments on the real plant. Since the tests were conducted under unfavorable conditions, the obtained data is not very extensive. However, it provides some insights into the potential and challenges of the proposed control design.

Finally, the last chapter summarizes the key findings, discusses conclusions, and provides suggestions for future improvements in the control design and the implementation at the Solar Tower Jülich.

2 Fundamentals

The following chapter will cover the fundamental aspects of solar tower power plants and outline the specifications of the Solar Tower Jülich. It will further introduce the underlying control theory, providing definitions for the model predictive control and moving horizon estimation algorithms. Additionally, the toolbox used in the implementation and a review of the existing literature on the control of solar tower power plants will be presented.

2.1 Solar Tower Power Plants

In solar tower power plants, the solar radiation is concentrated through a multitude of mirrors, so-called heliostats, onto a receiver placed on top of a tower. The receiver absorbs the solar radiation and transfers the energy to a heat transfer fluid (HTF). The heat can be used for power generation or energy storage. Figure 2.1 shows the general structure of a solar tower power plant, including the heliostat field, the receiver, an energy storage, and the energy conversion process.

The following sections will give a brief overview of the structure and function of the heliostat field and the receiver. The downstream processes will not be examined further, as they are not taken into account in the control algorithm considered in this thesis. Additionally, a short introduction to solar radiation as the primary energy source for solar tower power plants will be given.

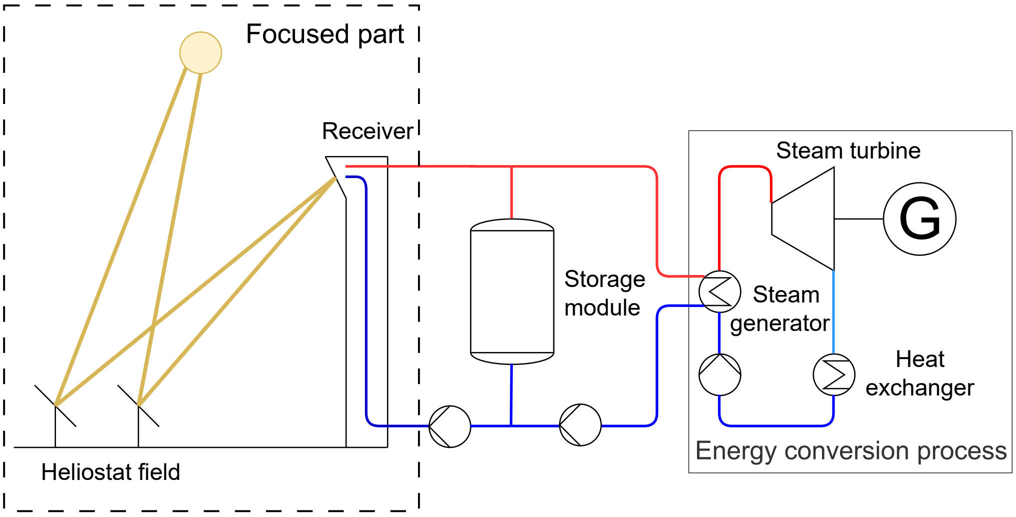

Figure 2.1: Schematic illustration of the operation principles and the subsystems in a solar tower power plant (Geschonneck, 2023).

2.1.1 Solar Radiation

The solar radiation that reaches the surface of the earth is referred to as global radiation, consisting of direct and diffuse radiation (see Figure 2.2). Diffuse radiation, resulting from the scattering of direct sunlight in the atmosphere, cannot be optically concentrated. Thus, only direct radiation is relevant for CSP systems. The average level of direct irradiance is highly dependent on the geographical location, as the sun's elevation angle changes with the latitude (Strauß, 2009). Table 2.1 shows the annual mean values for global, direct, and diffuse solar radiation for some selected locations.

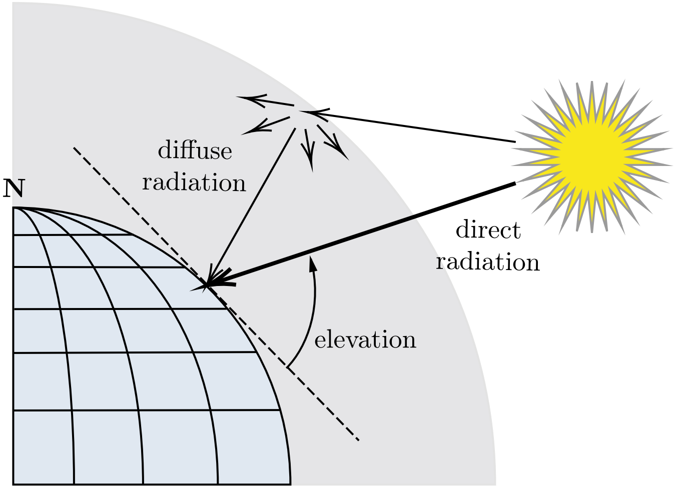

Figure 2.2: Illustration of the elevation angle and the direct and diffuse solar radiation.

Table 2.1: Annual mean values for global, direct and diffuse solar radiation for some selected locations in $\mathrm{kW\,h\,m^{-2}\,a^{-1}}$ (adapted from Strauß, 2009).

Location	Latitude	global radiation	direct radiation	diffuse radiation
Wadi Dhuliel (Jordan)	32°15′26″N	2113	1485	628
Almeria (Spain)	36°50′25″N	1784	1138	646
Stuttgart (Germany)	48°46′39″N	1138	631	507
Bergen (Norway)	60°23′22″N	785	315	470

In the field of solar energy systems, the Direct Normal Irradiance (DNI) is a commonly used metric for the design and operation of solar power plants. The DNI specifically refers to the solar irradiance received on a surface perpendicular to the incoming sunlight. The direct radiation does not only vary in dependence on the lateral distance to the equator. It also depends on other factors like the season, the time of day, the air pollution, and cloud conditions. The latter is especially relevant for the operation of solar power plants, as clouds can lead to rapid changes in the DNI, influencing the process temperatures, the safe operation, and the power output of the plant (Nouri et al., 2020).

2.1.2 Heliostat Field

The heliostat field consists of several, usually identical, heliostats that are arranged in rows or concentric circles (Belhomme, 2011). Two types of field layouts are prevalent, polar and surround fields, depicted in Figure 2.3. Due to the steepening angle of radiation and an increase of cosine losses (explained in Table 2.2), surround fields become less economic the closer a plant is located near the poles, making polar fields the favorable choice for such locations (Merchán et al., 2022). However, in general, surround fields have lower atmospheric losses, since the average distance between the heliostat and the receiver is shorter (Boretti et al., 2019).

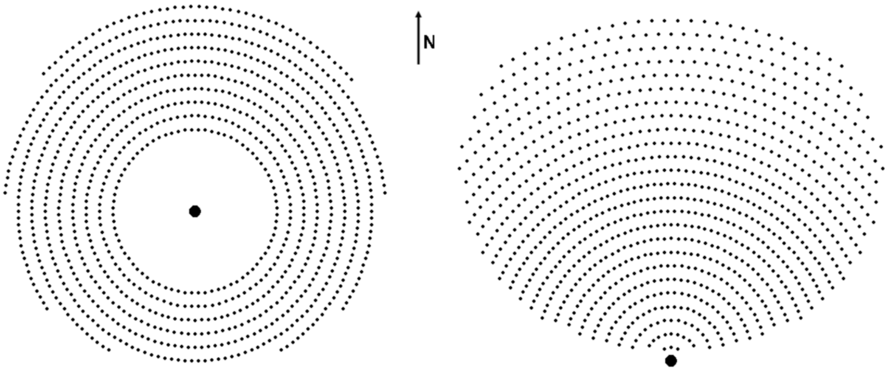

Figure 2.3: Heliostat field layouts in the northern hemisphere: surround field (left) and polar (north) field (right) (Belhomme, 2011).

Each heliostat consists of a support structure, and a reflective surface (often divided into several facets). With a tracking mechanism, the individual focal spot can be aligned with a target point on the tower during the course of the day. The number of heliostats, their sizes, and the arrangement within the field differ between power plants. The optimization in the design and the reduction of optical losses is still subject of current research projects (Merchán et al., 2022).

The redirecting of the available solar energy towards the receiver is not loss-free but subject to several constant as well as sun angle dependent optical losses. Table 2.2 summarizes the losses of the heliostat field. Some of them lead to a reduction of the reflected radiation. Others increase the spillage (reflected radiation that does not reach the receiver) due to a widening of the reflected image or a displacement of the aim points. In general, small heliostats lead to higher optical efficiencies of the field but are more expensive, as more heliostats need to be installed and controlled (Merchán et al., 2022).

2.1.3 Receiver

Placed on top of a tower, the receiver absorbs the solar radiation concentrated by the heliostat field and heats a heat transfer fluid.

Depending on the field layout, the receiver shape differs. For a surround field, the receiver is designed cylindrical. On the other hand, receivers for polar fields only absorb the radiation from one side and thus have an almost flat surface (see Figure 2.5).

Furthermore, a distinction between tubular and volumetric receivers can be made. Currently, the most prevalent type of receiver are tubular receiver, especially when using

Table 2.2: Optical losses of the heliostat field (adapted from Belhomme (2011))

Optical Loss	Description
Cosine losses	Highest optical loss. Reduction of effective reflection surface due to angle between sunlight and mirror normal.
Absorption losses	Absorption of a portion of the sunlight by the mirror, reducing the reflected radiation. Effect increases with dust and dirt on the surface. Absorption usually ranges between 6 % and 20 %.
Atmospheric losses	Absorption and scattering of the solar radiation by the atmosphere. Loss highly depends on the distance between heliostat and receiver.
Mirror error	Form deviation of the reflective surface (caused by manufacturing flaws, mechanical or thermal stresses) lead to imprecise aim points or wider reflections.
Shading	Heliostats are (partially) shaded due to objects (e.g. the tower, other heliostats) between the sun and the heliostat surface.
Blocking	Reflected radiation of one heliostat is (partially) blocked by another heliostat. Effect increases with lower sun angles and can be reduced by arranging the heliostats farther from each other.
Tracking error	Inaccuracy of the actuator in the tracking mechanism such that the heliostat does not align it's focal spot with the assigned target point on the tower.

a liquid HTF like molten salts (Merchán et al., 2022). They consist of vertical pipes carrying the HTF and absorbing the concentrated solar radiation depending on the surface material characteristics (Capuano et al., 2016). However, thermal losses due to large wall thicknesses and losses caused by reflection are known disadvantages (Capuano et al., 2016).

An alternative to tubular receivers are open volumetric receivers. Due to their porous structure, the radiation penetrates the entire volume of the receiver. This leads to a higher efficiency as less thermal radiation and reflection losses occur. Furthermore, the receiver surface is cooled by the HTF. It flows through the open volumetric structure causing the front side of the receiver to stay cooler than the evolving medium (Merchán et al., 2022).

Depending on the receiver and design of the power plant, several different heat transfer mediums are used within concentrated solar power systems, such as molten salt, water, liquid metals, particles, or air (Ding et al., 2021). Especially the use of air can be beneficial, as it is inexpensive, non-toxic, and can operate on high process temperatures, allowing higher-efficiency thermodynamic cycles (Capuano et al., 2016). However, the design of different receivers and development of suitable heat transfer mediums is still subject to current research projects (Ding et al., 2021).

Figure 2.4: The solar tower plant in Jülich. The left tower holds the receiver as well as the power conversion system. The right tower is used for research purposes and is not part of the power plant (DLR, n.d.).

Figure 2.5: The open volumetric receiver, with its 1080 ceramic absorber cups at the solar power plant in Jülich. The air shafts to the sides and the bottom of the receiver surface blow return air to the receiver surface to reduce wind influences (DLR, n.d.).

2.1.4 Solar Tower Jülich

The Solar Tower Jülich is a research facility of the German Aerospace Center (Deutsches Zentrum für Luft- und Raumfahrt, DLR) with a nominal capacity of 1.5 $\mathrm{MW_{el}}$. It was built in 2008 and has been used for research and development projects since. The solar plant in Jülich was one of the first solar power plants that used an open volumetric receiver and air as HTF (Gall, 2012). The solar tower and its heliostat field are depicted in Figure 2.4.

The plant consists of more than 2000 heliostats, each with a reflective surface of $8.3\,\mathrm{m}^2$ divided into four facets. The heliostats are arranged in a polar field to the north of the 60 m high tower. The tower carries the open volumetric receiver with a surface of $22.7\,\mathrm{m}^2$ ($4.35\,\mathrm{m} \times 5.22\,\mathrm{m}$), composed of 1080 ceramic absorber cups (Gall, 2012).

From the receiver surface, the air is sucked in through the absorber cups by a fan behind the receiver and heated up to 680 °C at a nominal mass flow of $9\,\mathrm{kg\,s^{-1}}$ (Gall, 2012). A steam generator inside the tower uses the high temperatures to convert water into steam, driving a steam turbine and a generator to produce electricity. Furthermore, the plant has a thermal storage system, with a capacity that allows about 1.5 hours of full-load operation of the power plant (Gall, 2012). Between the cups and to the sides of the receiver, air slots enable the returning air to circulate back to the front of the receiver, where it is mixed with ambient air and available to be heated up again (see Figure 2.5).

The solar tower plant in Jülich is equipped with several measurement devices, which allow the monitoring of the plant and the collection of data for research purposes. The surface temperature of the receiver is measured by an infrared thermographic camera, placed in front of the tower. Additionally, sensors are placed behind 108 of the 1080 absorber cups, measuring the air temperatures right after the ceramic cups. Another sensor determines the temperature of the combined mass flow at the outlet of the receiver. Moreover, the mass flow as well as the temperature of the air returning from the energy conversion (or storage) system are measured. On top of the tower, a pyrheliometer is placed to measure the solar direct radiation. Additionally, a short-term solar irradiance forecast system, referred to as nowcasting system, is implemented at the solar plant. It uses all-sky imagers to take snapshots of the sky at certain time intervals (Nouri et al., 2020). In combination with the DNI measurement from two pyrheliometers, the images are used to derive predicted DNI maps with a resolution of $20\mathrm{m} \times 20\mathrm{m}$ for a forecast horizon of up to 15 minutes (Samu et al., 2022).

A measurement of the solar flux density on the receiver surface, based on the reflections off the receiver, has been developed and installed as well. It is supposed to enhance the control by adding knowledge about the distribution of the solar radiation on the receiver surface. However, at the time of the experiments for this thesis, it has not been calibrated yet. Thus, a mock-up of the solar flux density measurement is implemented to be used until the final measurement system is operational.

2.2 Control Theory

A typical task in control engineering is the stabilization of operating points or the tracking of a reference trajectory in dynamical systems. In most applications, closed-loop controllers with a feedback of the measured system states are used. One of the most common control strategies in many industrial applications is the Proportional-Integral-Derivative (PID) controller due to its simplicity and reliability (Wang et al., 2012). However, with improvements in high-level software and computational power, advanced control strategies like model predictive control are becoming more popular and can enhance the performance of a control system significantly (Rawlings et al., 2020).

Depending on the availability of state measurements, the control system might require a state estimation. Several approaches on how to design a suitable state estimator exist. Apart from the state estimation, they can serve as a filter for process and measurement noise or estimate additional system parameters.

A well-established estimator for linear systems is the Kalman Filter. Extensions to the Kalman Filter, like the Extended Kalman Filter (EKF) (Welch et al., 2006) and the Unscented Kalman Filter (Julier et al., 1997), provide implementations for nonlinear systems. Furthermore, the Moving Horizon Estimator (MHE), which is used in this thesis, is able to operate on highly nonlinear and complex systems. A comparison of the MHE and the EKF for a nonlinear system is presented by Haseltine et al. (2005), where the MHE was shown to provide better state estimations. It further proved to be more robust to poor guesses of the initial state and tuning parameters.

In the following, the model predictive control algorithm as well as the definition of the moving horizon estimator are presented, as both are used for the control design in this thesis.

2.2.1 Model Predictive Control

Model Predictive Control (MPC) is an advanced control technique that uses a dynamic mathematical model of the system being controlled to make predictions about its future behavior. Unlike traditional control methods, which rely on predefined control laws, a model predictive controller continually optimizes the control actions over a finite time horizon by minimizing an objective function. Only the first control step of the resulting control input trajectory is applied to the system, as the optimization problem is repeatedly solved in every control step. As a notable advantage over other control strategies, model predictive control can handle state and input constraints by integrating them into the optimization problem. In the following, the model predictive algorithm is presented.

A discrete-time nonlinear system is given by

$$\mathbf{x}_{k+1} = f(\mathbf{x}_k, \mathbf{u}_k) \tag{2.1}$$

$$\mathbf{y}_k = h(\mathbf{x}_k), \tag{2.2}$$

with the states $\mathbf{x}_k \subseteq \mathbb{R}^n$, the inputs $\mathbf{u}_k \subseteq \mathbb{R}^m$ and the system outputs $\mathbf{y}_k \in \mathbb{R}^p$.

The corresponding optimal control problem at time t_n, given the current state $\mathbf{x}_n$ and the prediction horizon N can be described as

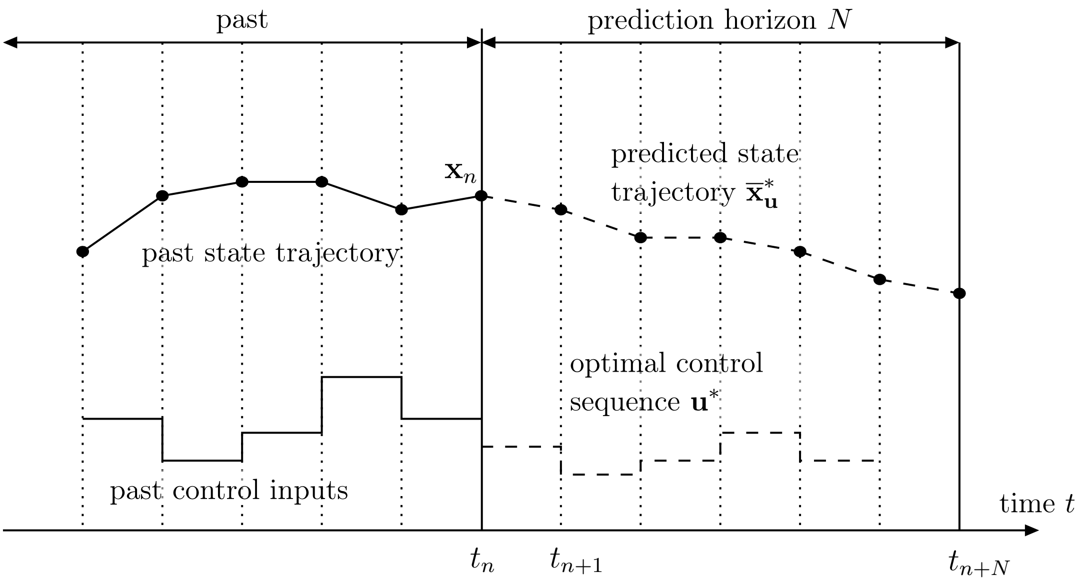

Figure 2.6: Illustration of the model predictive control algorithm (adapted from Grüne et al., 2011)

$$
\begin{aligned}
\min_{\mathbf{u}} \quad & M\left(\mathbf{x}_{\mathbf{u},N}\right) + \sum_{k=0}^{N-1} L\left(\mathbf{x}_{\mathbf{u},k}, \mathbf{u}_k\right) && && (2.3)\\
\text{subject to} \quad & \mathbf{x}_{\mathbf{u},0} = \mathbf{x}_n, && && (2.4)\\
& \mathbf{x}_{\mathbf{u},k+1} = f\left(\mathbf{x}_{\mathbf{u},k}, \mathbf{u}_k\right), && k = 0, \ldots, N-1 && (2.5)\\
& \mathbf{x}_{\text{lb}} \leq \mathbf{x}_{\mathbf{u},k} \leq \mathbf{x}_{\text{ub}}, && k = 0, \ldots, N && (2.6)\\
& \mathbf{u}_{\text{lb}} \leq \mathbf{u}_k \leq \mathbf{u}_{\text{ub}}, && k = 0, \ldots, N-1 && (2.7)
\end{aligned}
$$

with $\mathbf{x}_{\text{lb}}$, $\mathbf{x}_{\text{ub}}$, $\mathbf{u}_{\text{lb}}$ and $\mathbf{u}_{\text{ub}}$ denoting the state and input lower and upper bounds, respectively. $\mathbf{x}_{\mathbf{u}}$ denotes the predicted state trajectory resulting from the application of the input trajectory $\mathbf{u}$ to the system. The objective function consists of a terminal cost function M and a stage cost function L.

The solution to the optimization problem is the optimal input trajectory $\mathbf{u}^*_k$ for $k = 0, \ldots, N-1$, generating the optimal predicted trajectory $\bar{\mathbf{x}}^*_k$ for $k = 0, \ldots, N$. For the next iteration, only the first step of the optimal input trajectory $\mathbf{u}^*_0$ is applied to the system.

The idea of the MPC algorithm is also illustrated in Figure 2.6 and can be summarized in three steps:

- Step 1: At time t_n, measure state $\mathbf{x}_n$ and solve MPC optimization problem.
- Step 2: Apply $\mathbf{u}(t) := \mathbf{u}^*_0 \quad \forall t \in [t_n, t_n + t_{\text{step}}]$ to the system, with t_{step} being the sampling time.
- Step 3: Set $t_n = t_n + t_{\text{step}}$ and go to step 1.

The objective function as well as the set of constraints are subject to the controller design and can be adapted depending on the application. A common choice for the stage cost is the Euclidean norm of the tracking error between a reference trajectory $\mathbf{r}$ and the system output $\mathbf{y}$, given by

$$L\left(\mathbf{x}_{\mathbf{u},k}\right) = \left\| h(\mathbf{x}_{\mathbf{u},k}) - \mathbf{r}_k \right\|_2^2 = \left\| \mathbf{y}_{\mathbf{u},k} - \mathbf{r}_k \right\|_2^2 . \tag{2.8}$$

Furthermore, a penalty for the control inputs and the state derivatives might be reasonable and can be added to the objective function.

2.2.2 Moving Horizon Estimation

The Moving Horizon Estimator (MHE) formulates an optimization problem to estimate the states, and if necessary, parameters of the model. The structure of the optimization problem is similar to the one of the model predictive controller. However, instead of making predictions of the future, the MHE minimizes the difference between predicted and measured quantities over a finite time horizon in the past. It achieves this by adjusting the initial state and, if applicable, the model parameters. Like the MPC, the MHE can handle constraints and nonlinearities, which is a major advantage over other estimation techniques. For a nonlinear system

$$\mathbf{x}_{k+1} = f(\mathbf{x}_k, \mathbf{u}_k, \mathbf{p}) + \mathbf{w}_k \tag{2.9}$$

$$\mathbf{y}_k = h(\mathbf{x}_k, \mathbf{p}) + \mathbf{v}_k, \tag{2.10}$$

with the additive process and measurement noise $\mathbf{w}_k$ and $\mathbf{v}_k$, respectively as well as constant model parameters $\mathbf{p}$, the MHE optimization problem can be formulated as

$$\min_{\mathbf{x},\mathbf{p},\mathbf{v},\mathbf{w}} \quad \left\| \mathbf{x}_0 - \tilde{\mathbf{x}}_1 \right\|_{\mathbf{P}_\mathbf{x}}^2 + \left\| \mathbf{p} - \tilde{\mathbf{p}} \right\|_{\mathbf{P}_\mathbf{p}}^2 + \sum_{k=0}^{N-1} \left\| \mathbf{v}_k \right\|_{\mathbf{P}_\mathbf{v}}^2 + \left\| \mathbf{w}_k \right\|_{\mathbf{P}_\mathbf{w}}^2 \tag{2.11}$$

$$\text{subject to} \quad \mathbf{x}_{k+1} = f_k\left(\mathbf{x}_k, \mathbf{u}_k, \mathbf{p}\right) + \mathbf{w}_k, \qquad k = 0, \ldots, N-1 \tag{2.12}$$

$$\mathbf{y}_k = h(\mathbf{x}_k, \mathbf{p}) + \mathbf{v}_k, \qquad k = 0, \ldots, N-1 \tag{2.13}$$

$$\mathbf{g}_k\left(\mathbf{x}_k, \mathbf{u}_k, \mathbf{w}_k, \mathbf{p}\right) \leq 0, \qquad k = 0, \ldots, N-1 \tag{2.14}$$

with the weighting matrices $\mathbf{P}_\mathbf{x}, \mathbf{P}_\mathbf{p}, \mathbf{P}_\mathbf{v}, \mathbf{P}_\mathbf{w} \succeq 0$. The parameters $\tilde{\mathbf{p}}$ and the first state estimate $\tilde{\mathbf{x}}_1$ denote the results from the previous iteration. Additionally, $\mathbf{g}_k$ denotes general nonlinear constraints. Here, the penalty functions are chosen to be weighted Euclidean norms. However, other penalty functions can be used as well.

The optimal estimated parameters $\mathbf{p}$ result directly from the optimization. The current state estimate can be calculated by the evaluation of the system dynamics.

The process is repeated for every control step. Figure 2.7 illustrates the quantities and the idea of the MHE algorithm.

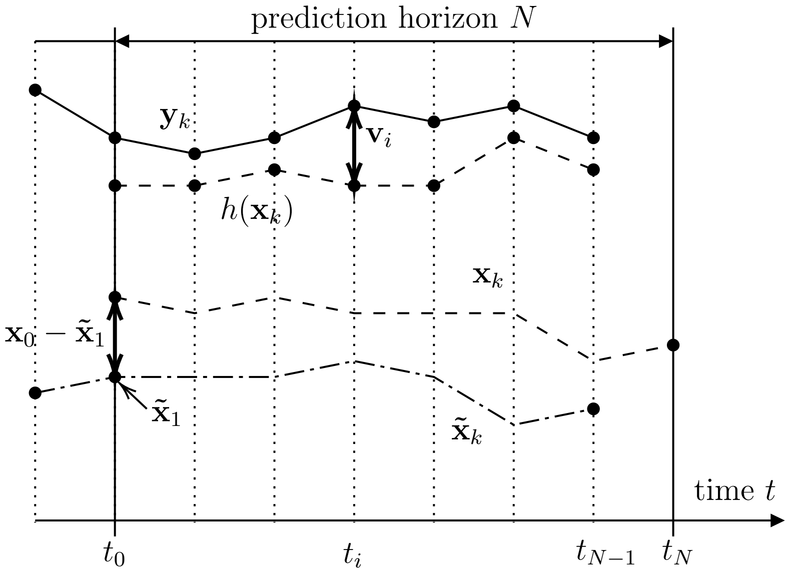

Figure 2.7: Illustration of the moving horizon estimator algorithm. Depicted are the trajectories of the measured output values $\mathbf{y}_k$ and the output values calculated by the model $h(\mathbf{x}_k)$. They differ by the measurement noise v_k. The trajectory of the estimated states $\mathbf{x}_k$ based on the initial state value $\mathbf{x}_0$ and the estimated state trajectory from the previous iteration $\tilde{\mathbf{x}}_k$ are illustrated underneath.

2.3 do-mpc Toolbox

The do-mpc software is a Python-based model predictive control toolbox (do-mpc, 2022). It is an open-source project developed in 2014 by researchers at the TU Dortmund with the goal of providing a modular, user-friendly, and easy-to-use toolbox for nonlinear model predictive control (Lucia et al., 2014). The toolbox is based on CasADi, a software tool that facilitates the efficient solution of nonlinear optimization problems (Andersson et al., 2019). The implementation of do-mpc consists of simulation, estimation, and control components that can be used individually or in combination. For each component, the user can implement a model. They can be formulated with continuous ordinary differential equations, differential algebraic equations, or discrete equations. Additionally, the user defines the optimization problems for the estimation and control components.

The estimation functionality of the do-mpc toolbox implements a moving horizon estimator (see Chapter 2.2.2) that can be used to estimate the states $\mathbf{x}$ and parameters $\mathbf{p}$ of the model.

2.4 Existing Approaches for the Control of Solar Tower Power Plants

Numerous approaches for the automatic control of solar tower power plants have been proposed in the past. Especially the optimal aim point control of the heliostats has been subject to many research projects, yielding a variety of different control strategies. Some of them feature open-loop controllers, without the ability to compensate for modeling errors, like mirror and tracking errors or disturbances such as clouds. For example, Belhomme, Pitz-Paal, and Schwarzbözl (2014) proposed an open-loop strategy based on the ant colony optimization metaheuristic in combination with a ray tracing tool (`STRAL`) calculating the solar flux density distribution on the receiver.

Several closed-loop controllers have been proposed as well. Vant-Hull et al. (1996) developed the Dynamic Aimpoint Processing System (DAPS), a search and replace algorithm that detects "hot spots" on the receiver exceeding the allowable flux density (AFD). It identifies the heliostats with the greatest influence and defocuses them. The DAPS algorithm was successfully implemented in 1997 at the *Solar Two* plant in Barstow (CA, USA). García, Soo Too, et al. (2018) proposed an aim point strategy based on a multivariable model predictive control approach. It is a closed-loop control procedure, using focusing parameters as control inputs such that the solar irradiance is distributed over the central receiver according to the predefined heat flux limits.

A recent overview of several different approaches can be found in (Zhu et al., 2023). A lot of the approaches concentrate on the optical performance of the heliostat field, aiming for a homogeneous flux density distribution on the receiver instead of maximizing the overall achieved receiver power. Additionally, only a few authors explicitly address cloud disturbances and tested the proposed strategies under these conditions.

Crespi et al. (2018) simulated the performance of different aim point strategies under the influence of passing clouds on a receiver operating on molten salts. They defined several cloud scenarios, varying in the amount of clouds, their sizes, and the part of the heliostat field that is covered. Furthermore, they incorporated the control system of the solar receiver into the simulations, which adjusts the mass flow rate of the molten salt based on a feedback controller. They found, that the same clouds can have very different effects dependent on *where* the cloud is covering the heliostats and *when* during the day the cloud occurs. Furthermore, their simulations showed that scenarios with high cloud coverages lead to oscillations in the outlet temperature, induced by the mass flow control, occur during the unshading.

García, Barraza, et al. (2022) proposed a closed-loop control strategy to maintain the outlet fluid temperature during DNI fluctuations by manipulating both the mass flow rate and the heliostat aim points. The control strategy combines three controllers: one controller for the control of the heliostat aim points to keep the solar flux under the allowable flux density on the receiver, a feedforward controller to compensate for the DNI variations, and a feedback controller to maintain the outlet temperature. The control system is based on the use of intermediate flow valves along the HTF flow path to reduce time delay and to make the control system more responsive to DNI variations. The proposed strategy was tested in simulation on a solar plant model with a surround field and a cylindrical receiver, using molten salt as the HTF. The proposed strategy achieved over 80% improvement in simulation compared to conventional single-loop temperature controls.

Zhu et al. (2023) proposed a model predictive control approach providing a heliostat field aiming strategy based on predicted solar flux distributions using cloud shadowing forecasts. The aiming strategy was formulated as an optimization problem minimizing the deviation between a reference flux trajectory and the actual solar flux on the receiver, subject to the allowable flux density. In order to take into account the adjustment energy of the heliostats in the optimization, hard constraints on the adjustment angles of the heliostats were imposed. The proposed method was tested on a field sector at the Noor Power Station in Morocco for a range of cloud scenarios. The results demonstrated the effectiveness of the method compared to other aim point strategies.

Model Predictive Control Design for the Solar Tower Jülich The most recent work at the Solar Tower Jülich has been presented by Geschonneck (2023), designing a model predictive controller. The aim was to control the outlet temperature during cloud disturbances by the combined control of the heliostat aim points and the mass flow. The cloud predictions for the controller were based on the nowcasting system available at the site in Jülich.

As aim point strategy, the designed controller applies an approximation of the valve analogy algorithm introduced by García, Soo Too, et al. (2018). This way the control inputs for the aim point control were reduced to three so-called dispersion factors and complemented by the mass flow control input. Due to the resolution of the nowcasting system, the heliostats are divided into groups of heliostats covering an area of $20\,\mathrm{m} \times 20\,\mathrm{m}$. Each of the groups has a representative heliostat, that is used for the aim point control.

The quality of the control was measured in simulations evaluating the Root Mean Square Error (RMSE) between the air outlet temperature and the reference temperature at nominal load. Furthermore, the performance and robustness were compared for different uncertainties in the cloud predictions. For each simulation, a cloud scenario was formulated consisting of a predicted cloud $\mathrm{Cloud}_{\mathrm{pred}}$, used as the cloud forecast data, and the simulated cloud $\mathrm{Cloud}_{\mathrm{sim}}$, representing the actual cloud passage. Each cloud was specified by a start time, the duration, the cloud speed, and the shading, defined as the intensity of the solar irradiance drop. The shading depends on the size and the transmissivity of the cloud. Additionally, a ramp length for the transition between the shaded and unshaded state can be defined. The parameters of the cloud definition are depicted in Figure 2.8.

If the predicted cloud and the simulated cloud are identical, the controller is tested under the influence of an exact cloud forecast. If the predicted and simulated clouds differ from each other, the influence of an inaccurate cloud forecast is tested and the robustness of the control can be evaluated.

The simulations showed that compared to a reference scenario, where the control parameters were set constant, a change in the outlet temperature can be reduced by up to 86.4 % if the cloud prediction is exact. The control was particularly effective at low shading intensities. It was able to ensure safe operation by limiting the receiver surface temperature to the maximum allowed values for a wide range of cloud speed and light transmittance predictions. However, with a predicted cloud where the cloud speed is assumed to be more than $-11\,\%$ slower than the simulated cloud, the controller was not able to maintain the outlet temperature within the allowed range. Similar results were obtained for the case of an inaccurate prediction of the cloud's transmissivity. A false

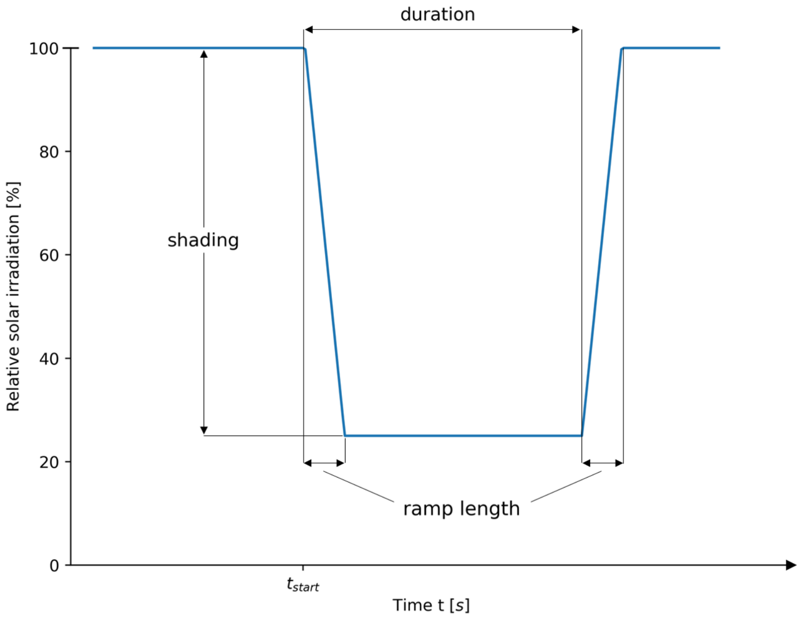

Figure 2.8: Illustration of the parameters used for a cloud definition in the simulations (Geschonneck, 2023).

prediction of more than $-5\,\%$ resulted in a temperature deviation outside the allowed range. Nevertheless, the simulations showed that the implemented control was able to increase the efficiency during cloud passages and reduce the temperature changes for a wide range of cloud scenarios.

3 Modeling

As a basis for the optimization in the model predictive controller and the moving horizon estimator, a model of the system is required. Different models have been used for the various research projects at the solar plant in Jülich so far. For the before-mentioned model predictive controller design by Geschonneck (2023) a physical model of the system has been implemented. Most parts of the model are used in this thesis as well, however some parts have been subject to adaptions within the development process at the DLR. The updated model is presented in the following, divided into the three subsystems

- Heliostat field
- Receiver, including:
    - Absorber cups
    - Header
- Fan.

The receiver model has been replaced completely by a polynomial model due to better accuracies. The previous physical receiver model used by Geschonneck (2023) is described in Appendix A.1, as it provides a comprehensive understanding of the physical setup and might still be used for future control designs.

As not all receiver cups are modeled individually, the model reduction to a subset of 30 cups and the coupling of the subsystems is explained. Furthermore, the cloud representation used for the simulations and experiments later in the thesis will be described briefly.

3.1 Heliostat Field

The heliostat field model describes the optical properties of the system and can be divided into the subparts *aim point strategy* and *flux density approximation*, as shown in Figure 3.1. It determines the aim points for the heliostats and a map of solar flux values for each simulated cup. For this, the heliostat field model uses two inputs $\mathbf{u} = [\kappa_1, \kappa_2]^T$ and the current DNI value, implemented as time-varying parameter.

Aim Point Strategy Due to the large number of heliostats in the field an individual control input for each heliostat would be computationally expensive and not feasible for a real-time control. Instead, a mapping from a reduced number of control inputs $\mathbf{u} \in \mathbb{R}^m$ to an aim point of each heliostat is introduced and referred to as the aim point strategy.

As described in Chapter 2.4 several aim point strategies have been developed in the past. For the MPC design and simulations by Geschonneck (2023), the aim point strategy introduced by García, Soo Too, et al. (2018) was used and modified to fit the specifications and needs of the solar plant in Jülich. The strategy is referred to as *valve analogy* and divides the field into groups of heliostats depending on their distance to the receiver. The

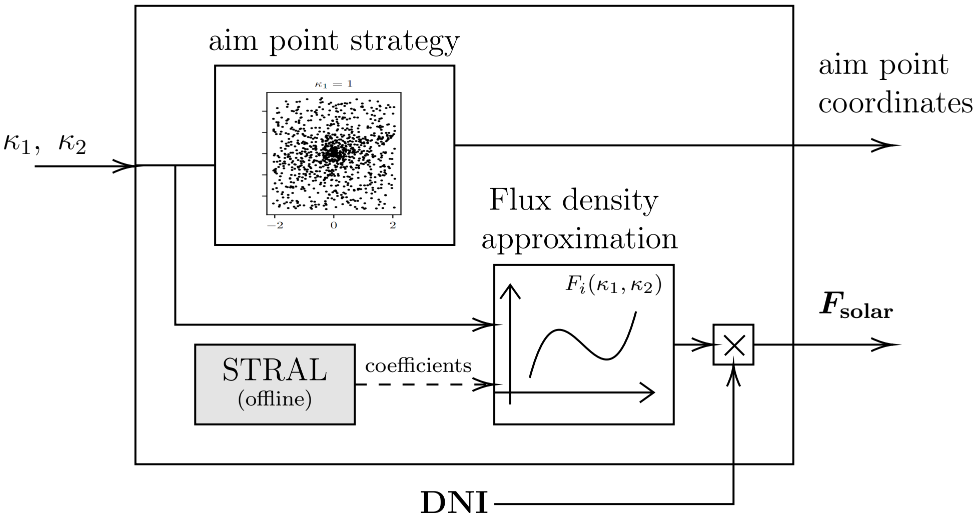

Figure 3.1: Illustration of the elements of the heliostat field model.

aim points of each group are controlled by a single control input, called dispersion factor. As the name suggests, the higher the factor, the more spread out the aim points are over the receiver surface.

Even though the valve analogy showed good results in the simulations, an alternative aim point strategy was implemented for the use in the experiment setup (Zanger, 2023). It reduces the number of control inputs even further, defining a mapping from two control inputs

$$\kappa_1 \in [0.5, 2.5] \tag{3.1}$$

$$\kappa_2 \in [0, 1] \tag{3.2}$$

to the aim point coordinates for all heliostats. The first control input κ_1 defines how much the individual aim points are dispersed over the receiver surface, whereas κ_2 sets the proportion of heliostats used to concentrate the radiation on the receiver. With $n_{\text{heliostats}}$ being the total number of heliostats in the field, the number of heliostats used to concentrate solar radiation on the receiver can be expressed by

$$n_{\text{heliostats,focused}} = \text{round}\ \kappa_2 \cdot n_{\text{heliostats}}. \tag{3.3}$$

The selection of heliostats to be included in the focused set is subject to a random pick. With the large number of heliostats, it can be assumed that the chosen heliostats will be distributed evenly over the field, thus always yielding comparable flux density distributions. The other heliostats will defocus and aim to a predefined off-receiver point.

For the calculation of the aim points for the focused heliostats, each aim point is defined in polar coordinates (r_i, φ_i) first. The center of the coordinate system aligns with the center of the receiver. For a radially uniform distribution of aim points, the angle φ_i of each aim point $i \in \{0, 1, \ldots, n_{\text{heliostats,focused}} - 1\}$ is set to

$$\varphi_i = \frac{2\pi i}{n_{\text{heliostats,focused}}}. \tag{3.4}$$

The assignment of the radius for each point is performed through a random process. First, a random number $\hat{r}_i$ between 0 and 1 is generated, following a standard uniform

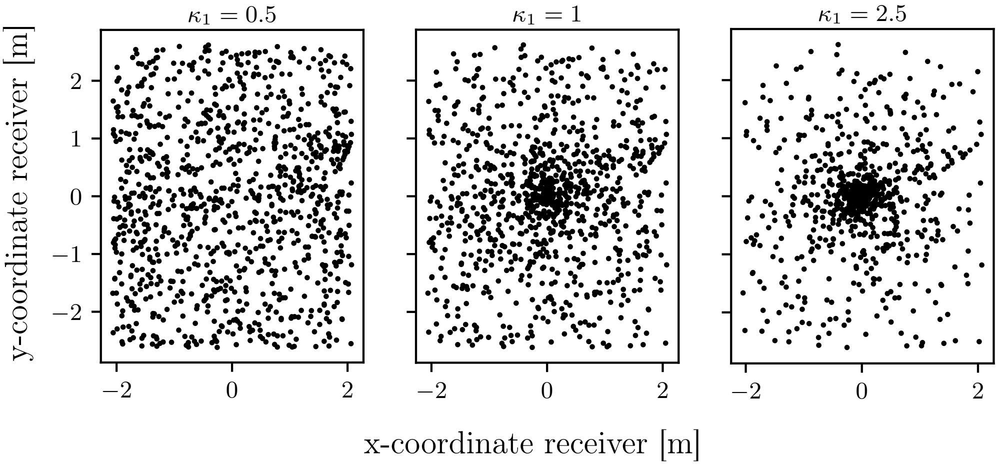

Figure 3.2: Aim point distribution for different values of κ_1.

distribution $U(0, 1)$:

$$\hat{r}_i \sim U(0,1) \tag{3.5}$$

Then, each sampled value is raised to the power of κ_1 by applying

$$r_i = \hat{r}_i^{\,\kappa_1}. \tag{3.6}$$

This way, for $\kappa_1 = 1$ the points are uniformly distributed over the unit circle. Values of $\kappa_1 < 1$ lead to a more centered distribution, whereas values with $\kappa_1 > 1$ distribute the points closer to the edges. In order to project the distributed aim points from the unit circle to the rectangular receiver surface, the new radius is calculated by

$$r(\varphi_i) = \begin{cases} \frac{a}{|\cos\varphi_i|}, & |\tan\varphi_i| \le \frac{b}{a} \\ \frac{b}{|\sin\varphi_i|}, & |\tan\varphi_i| \ge \frac{b}{a}, \end{cases} \tag{3.7}$$

with a and b being half the lengths of the receiver in x- and y-direction, respectively.

The coordinates of the aim points are then retrieved by transforming the polar coordinates to cartesian coordinates, using

$$\begin{aligned} x_i &= r_i \cdot \cos(\varphi_i) \\ y_i &= r_i \cdot \sin(\varphi_i). \end{aligned} \tag{3.8}$$

The operating system of the heliostats (HeliOS) operates on a discrete set of 1080 heliostat aim points, corresponding to the center points of the absorber cups. Thus, in the last step, the calculated aim points get assigned to the nearest aim point defined in HeliOS.

Figure 3.2 shows the resulting aim point distribution for 1000 heliostats and different values of κ_1.

Flux Density Approximation The second part of the optical model approximates the flux density that reaches the simulated absorber cups when applying the control inputs κ_1 and κ_2. These flux densities can be simulated using the ray tracing tool STRAL (Solar

Tower Ray Tracing Laboratory). It has been developed by the DLR (Belhomme, Pitz-Paal, Schwarzbözl, and Ulmer, 2009) and uses the geometry data of the heliostats in the field to calculate the flux density distribution on the receiver. Furthermore, it considers all optical losses that were described in Table 2.2.

For the use in the model, `STRAL` cannot be used directly as its functionality is not differentiable. Instead, `STRAL` is applied offline to calculate the flux densities on the receiver for various values of κ_1 and different sun positions dependent on the time of day. The obtained flux density distributions are then used in a least square regression to fit the polynomial coefficients of a third-order polynomial for each simulated absorber cup. With a normalization to a DNI value of $1\,\mathrm{W\,m^{-2}}$, the resulting approximation of the flux densities at absorber cup i is given by

$$F_{\text{solar}}i(\kappa_1, \kappa_2) = \kappa_2 \cdot (c_{0,i} + c_{1,i} \cdot \kappa_1 + c_{2,i} \cdot \kappa_1^2 + c_{3,i} \cdot \kappa_1^3). \tag{3.9}$$

3.2 Receiver

The open volumetric receiver used at the Solar Tower Jülich, consists of 1080 ceramic absorber cups, which are grouped in four sectors. Each cup consists of a receiver comb, a receiver tub, and the tubing, as shown in Figure 3.3. The receiver comb absorbs the concentrated solar radiation and transforms it into thermal energy. The porous structure of the ceramic material allows the air to flow through the receiver comb and absorb the heat. The different temperatures and heat flows, especially needed for the physical model, are depicted in Figure 3.4.

The tub and tubing forward the air towards the headers, a cascade of two funnel structures, where the enthalpy flows of the individual cups are combined and homogenized to one air flow. The mass flow through each absorber cup is dependent on the diameter of an orifice plate at the end of the tubing. This way the absorber cups near the center of the receiver can benefit from higher mass flows, as they need more cooling due to a higher concentration of solar radiation in the center.

After the secondary header, the heated air exits the receiver and is used for the downstream process, where it cools down and is then recirculated to the receiver to benefit from the remaining heat. To increase the efficiency of the receiver, the returning air is blown through air gaps between the absorber cups in front of the receiver and is then

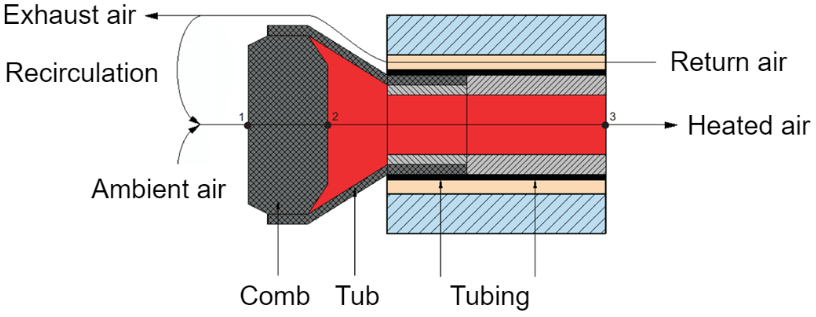

Figure 3.3: Schematic illustration of the structure of one absorber cup (Geschonneck, 2023).

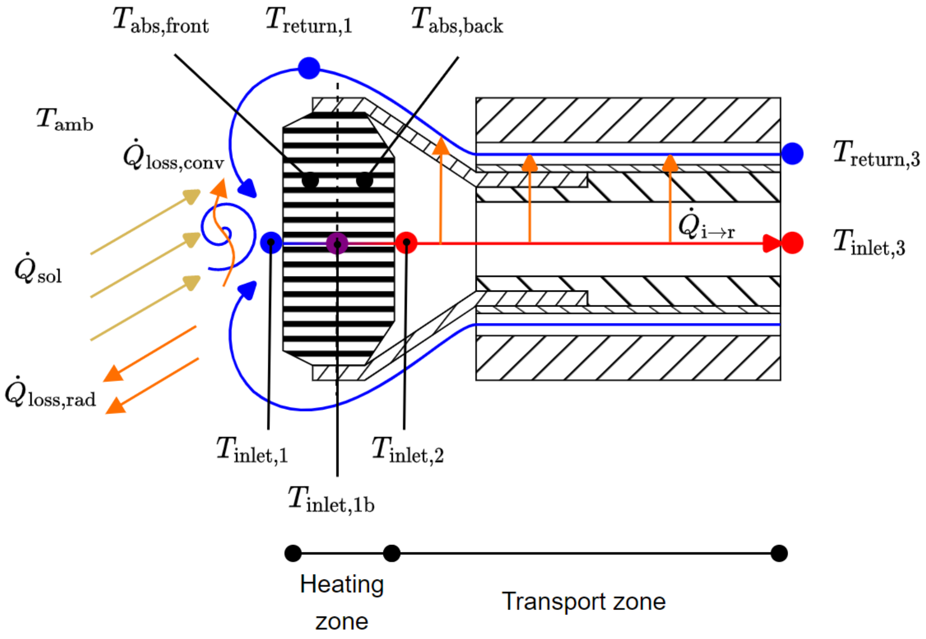

Figure 3.4: Illustration of the variables of the absorber cup (Geschonneck, 2023).

reused in the process. The individual absorber cups are assumed to be thermally isolated from each other so that each absorber cup can be modeled individually.

In the following, the used model for the absorber cups and the header are described.

3.2.1 Absorber Cup

The model used for the previous MPC design by Geschonneck (2023) is a physical model introduced by Gall (2012) and developed further by Iding et al. (2023). It uses the two system states $T_{\text{abs,back}}$ and $T_{\text{abs,back}}$ as well as two algebraic states $T_{\text{inlet},1b}$ and $T_{\text{inlet,2}}$, depicted in Figure 3.4. For reference, the model is further explained in Appendix A.1.

As an alternative approach to the physical model, measurement data from previous experiments were used for the fitting of a polynomial model by Zanger (2023). The steady-states $x_{ss} = [T_{\text{abs,front,ss}}, T_{\text{inlet,3,ss}}]^T$ were approximated by

$$T_{\text{abs,front,ss}} = c_1 \cdot \dot{m} + c_2 \cdot F_{\text{solar}} + c_3 \cdot T_{\text{return,3}} + c_4 \tag{3.10}$$
$$T_{\text{inlet,3,ss}} = c_6 \cdot \dot{m} + c_7 \cdot F_{\text{solar}} + c_8 \cdot T_{\text{return,3}} + c_9, \tag{3.11}$$

with c_i being constant coefficients resulting from the fitting process. The used temperatures are also displayed in Figure 3.4.

The differential equations for the model are then approximated by

$$\dot{T}_{\text{abs,front}} = c_0 \cdot (T_{\text{abs,front,ss}} - T_{\text{abs,front}}) \tag{3.12}$$
$$\dot{T}_{\text{inlet,3}} = c_5 \cdot (T_{\text{inlet,3,ss}} - T_{\text{inlet,3}}), \tag{3.13}$$

with c_0 and c_5 being the time constants resulting from the fitting.

By introducing additional parameters p_i the model can be adjusted to account for fitting errors or other model disturbances. For the dynamic model constants, it was chosen to replace the constants entirely by the parameters. However, for the steady-state constants, the parameters adapt the corresponding constant. This results in

$$\dot{T}_{\text{abs,front}} = p_0 \cdot (T_{\text{abs,front,ss}} - T_{\text{abs,front}}) \tag{3.14}$$

$$\dot{T}_{\text{inlet,3}} = p_5 \cdot (T_{\text{inlet,3,ss}} - T_{\text{inlet,3}}), \tag{3.15}$$

with the steady-states approximated by

$$T_{\text{abs,front,ss}} = (c_1 + p_1)\dot{m} + (c_2 + p_2)F_{\text{solar}} + (c_3 + p_3)T_{\text{return,3}} + (c_4 + p_4) \tag{3.16}$$

$$T_{\text{inlet,3,ss}} = (c_6 + p_6)\dot{m} + (c_7 + p_7)F_{\text{solar}} + (c_8 + p_8)T_{\text{return,3}} + (c_9 + p_9). \tag{3.17}$$

Consequently, a parametrization with

$$p_i = \begin{cases} c_i & \text{for } i \in \{0, 5\} \\ 0 & \text{for } i \in \{1, \dots, 4\} \cup \{6, \dots, 9\} \end{cases} \tag{3.18}$$

represents the model behavior that resulted from the fitting process.

Model Comparison With the use of the polynomial model instead of the physical model, the system states of the receiver model have changed, as displayed in Table 3.1.

Table 3.1: Comparison of the states used in the physical model and polynomial model of the receiver.

Variable	physical model	polynomial model
states $\mathbf{x}$	$T_{\text{abs,front}}$	$T_{\text{abs,front}}$
	$T_{\text{abs,back}}$	$T_{\text{inlet,3}}$
algebraic states $\mathbf{z}$	$T_{\text{inlet,2}}$	-
	$T_{\text{inlet,1}b}$	-

An advantage of using $T_{\text{inlet,3}}$ instead of $T_{\text{abs,back}}$, is the availability of measurements for $T_{\text{inlet,3}}$ for a selected set of cups, thus no state estimation is mandatory anymore. Additionally, the model reduces in complexity and no algebraic states are needed.

An analysis of the model accuracies for a set of measured test data showed that the polynomial model was able to represent the system behavior better than the physical model. For the comparison, RMSE values were calculated as a sum of the RMSE values of $T_{\text{abs,front}}$ and $T_{\text{inlet,3}}$ for each cup. The polynomial model achieved an RMSE value of 10.1 K whereas the physical model yielded an RMSE value of 22.3 K (Zanger, 2023). Due to this significant improvement in accuracy, it was chosen to change the implemented model of the MPC to the polynomial receiver model.

3.2.2 Header

As mentioned before, the header combines and homogenizes the enthalpy flows coming from the four sectors of the absorber cups. It is composed of two parts, the first and the secondary header. Figure 3.5 shows the serial layout of the headers.

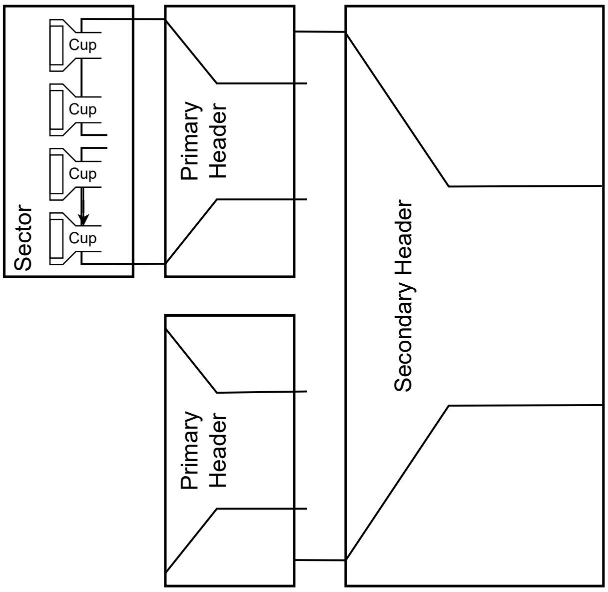

Figure 3.5: Schematic illustration of the header parts (Geschonneck, 2023).

Without losses in the header, the enthalpy flow resulting from combining the flows of n_{cups} can be described with

$$\dot{H}_{\mathrm{inlet,3,mixed}} = \sum_{i=1}^{n_{\mathrm{cups}}} \dot{m}_{\mathrm{abs},i} \cdot h_{\mathrm{inlet,3},i}(T_{\mathrm{inlet,3},i}). \tag{3.19}$$

The equation uses a predefined third-order polynomial approximating the specific enthalpy h of dry air as a function of the air temperature T.

Additionally, losses in both headers can be considered by introducing a heat flow $\dot{Q}_{\mathrm{loss}}$ for each header. The enthalpy flow after the primary header is then described by

$$\dot{H}_{\mathrm{sector}} = \dot{H}_{\mathrm{inlet,3,mixed}} + \dot{Q}_{\mathrm{loss,header,1}} \tag{3.20}$$

followed by the outlet enthalpy flow

$$\dot{H}_{\mathrm{out}} = \dot{H}_{\mathrm{sector,mixed}} + \dot{Q}_{\mathrm{loss,header,2}}. \tag{3.21}$$

The specific enthalpy is given by

$$h_{\mathrm{out}} = h_{\mathrm{sector,mixed}} + \frac{\dot{Q}_{\mathrm{loss,header,2}}}{\dot{m}_{\mathrm{rec}}}, \tag{3.22}$$

with $\dot{m}_{\mathrm{rec}}$ denoting the total mass flow through the receiver. The outlet temperature $T_{\mathrm{out}}(h_{\mathrm{out}})$ is calculated by inverting the previously mentioned polynomial approximation for the specific enthalpy. As described by Geschonneck (2023) the losses $\dot{Q}_{\mathrm{loss,header,1}}$ and $\dot{Q}_{\mathrm{loss,header,2}}$ are dependent on the dimensions of the header, the temperature difference between the header and the ambient air as well as the thermal conductivity of the material (see appendix A.1).

3.3 Fan

The Solar Tower Jülich uses air as a heat transfer medium. For generating and controlling the required air mass flow, two blower/valve combinations are part of the plant, one controlling the air flow through the receiver and the other controlling the mass flow through the storage and power generation system. The ratio of the volumetric air flows in these subsystems determines if the storage is charged or discharged. Additionally, it defines if the power generation process is using the heated air from the receiver or stored heat from the storage (Gall, 2012). Since the power generation process is not part of the model and is also not used in the experimental setup, only the first blower/valve combination influencing the mass flow through the receiver was considered in the model. Since the interaction between the valve and blower results in a damped oscillation when setpoint changes occur, a second-order system was used to model the behavior (Geschonneck, 2023). The differential equation is given by

$$K_p \dot{m}_{\text{setpoint}}(t) = T^2 \frac{\mathrm{d}^2 \dot{m}_{\text{rec}}}{\mathrm{d}t^2} + 2DT \frac{\mathrm{d}\dot{m}_{\text{rec}}}{\mathrm{d}t} + \dot{m}_{\text{rec}}. \tag{3.23}$$

To determine the time constant T, the damping constant D, and the proportional gain K_P, Geschonneck (2023) analysed measurements of step responses from the system, resulting in

$$\begin{aligned} K_P &= 3,55 \cdot 10^{-4} \frac{\text{kg h}}{\text{s m}^3} \\ T &= 11,60\text{s} \\ D &= 0,35. \end{aligned} \tag{3.24}$$

For the use in the implementation, the second-order differential equation stated in Equation 3.23 has been converted into a set of two first-order differential equations given by

$$\begin{aligned} \dot{x}_1 &= x_2 \\ T^2 \dot{x}_2 &= K_p \dot{m}_{\text{setpoint}}(t) - 2DTx_2 - x_1, \end{aligned} \tag{3.25}$$

introducing the states $x_1 = \dot{m}_{\text{rec}}$ and $x_2 = \ddot{m}_{\text{rec}}$.

3.4 Model Setup

The above-mentioned model parts are implemented individually and then coupled, as displayed in Figure 3.6. First, the inputs κ_1, κ_2, and $\dot{m}_{\text{setpoint}}$ are applied to the heliostat field model and the fan. The resulting outputs of these subsystems provide the inputs to the receiver model. Additionally, the measured variable $T_{\text{return,3}}$ is used by the receiver model. However, not all measured variables used in the model parts, or later in the controller are depicted. Thus, Table 3.2 summarizes the measured quantities and their usage in the model and the control setup, which will be further described in Chapter 4.

The general setup and coupling of the model are taken from the implementation by Geschonneck (2023) and Zanger (2023). The resulting states of the coupled model are given by

$$\mathbf{x} = [\boldsymbol{T}_{\textbf{abs,front}}, \boldsymbol{T}_{\textbf{inlet,3}}, \dot{m}_{\text{rec}}, \ddot{m}_{\text{rec}}]^T. \tag{3.26}$$

Table 3.2: Measurements used in the model and control setup.

Measurement	Usage
$\boldsymbol{T}_{\mathbf{abs,front}}$	measured system output
$\boldsymbol{T}_{\mathbf{inlet,3}}$	measured system output
$\dot{m}_{\mathrm{rec}}$	measured system output
T_{out}	used in the objective function
$T_{\mathrm{return,3}}$	used in the objective function, input to polynomial receiver model
$\boldsymbol{F}_{\mathbf{solar}}$	input to polynomial receiver model
DNI	used for the flux density calculation in the heliostat field model
available heliostats	used to adapt the bound on κ_2 in the heliostat field model

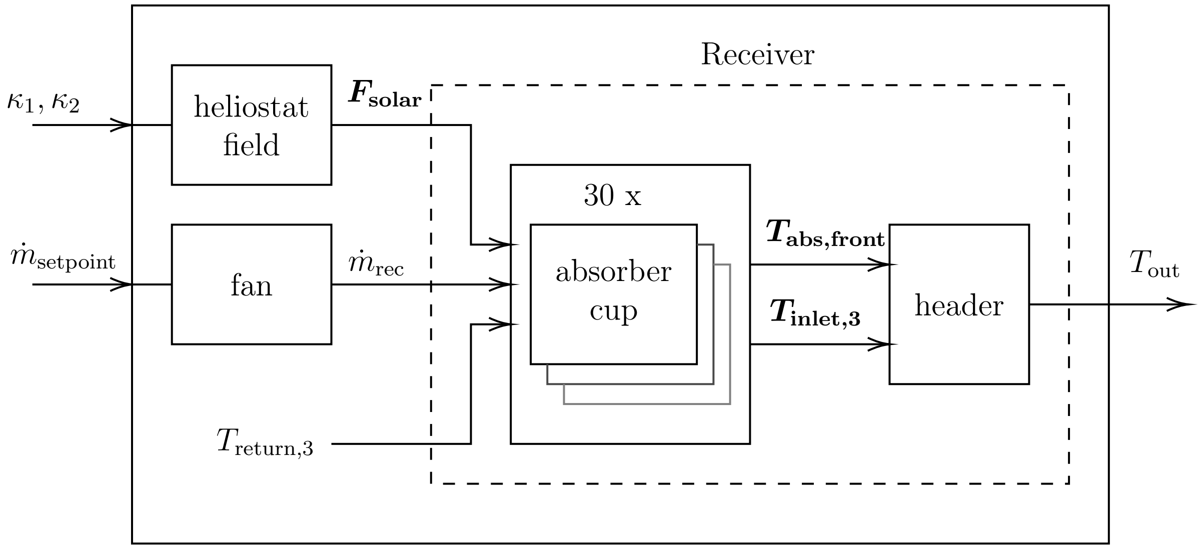

Figure 3.6: Coupling of the model subsystems.

The second derivative of the mass flow ($\ddot{m}_{\mathrm{rec}}$) is determined by a discrete approximation using the finite difference of the mass flow $\dot{m}_{\mathrm{rec}}$. Due to the applied sampling time of 10 s, the time intervals are sufficiently large to avoid high-frequency noise on $\ddot{m}_{\mathrm{rec}}$. Thus, no additional filtering is required.

As the receiver consists of 1080 absorber cups, modeling all cups would result in a high dimensional model and high computational cost when applied in the MPC. Therefore, the model is reduced by grouping the absorber cups into 30 sectors, each consisting of 36 absorber cups. In each sector, one absorber cup is modeled, assuming that the temperatures of the surrounding cups in the sector are homogeneous. The choice of the representative cups to be modeled is based on the available temperature sensors measuring $T_{\mathrm{inlet,3}}$ placed behind the absorber cups, while also trying to distribute the representative cups evenly over the receiver surface.

For the control setup used in the simulations and experiments, Figure 3.7 depicts the chosen distribution of representative cups on the receiver surface. Highlighted is the Cup

15 in the receiver center, which will be referred to in later chapters.

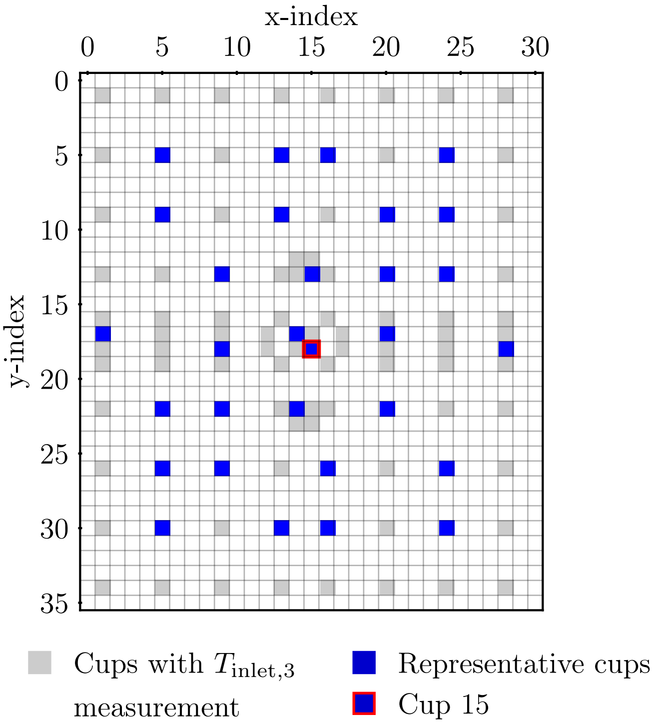

Figure 3.7: Choice of 30 out of 1080 absorber cups modeled in the control setup.

In order to determine a reduced mass flow value that represents the portion flowing through the 30 simulated cups, a conversion factor $\mu_{\dot{m}}$ is determined.

The mass flow $\dot{m}$ through a tube is defined as

$$\dot{m} = \rho \cdot A \cdot v, \tag{3.27}$$

with the density ρ, the velocity v, and the cross section area $A = \pi \cdot \left(\frac{d}{2}\right)^2$, considering the tube diameter d. Assuming a constant air density and velocity, the reduced mass flow through the 30 chosen cups, each with the corresponding orifice diameters $d_{\text{chosen},i}$ can be calculated by

$$\begin{aligned} \dot{m}_{rec,red} &= \frac{\sum_{i=1}^{30} d_{\text{chosen},i}^2}{\sum_{j=1}^{1080} d_j^2} \cdot \dot{m}_{\text{rec}} && (3.28) \\ &= \mu_{\dot{m}} \cdot \dot{m}_{\text{rec}}. && (3.29) \end{aligned}$$

The orifice diameter of each cup is denoted by d_j. $\mu_{\dot{m}}$ is the newly introduced mass flow ratio. The mass flow ratio is applied in the controller to first reduce the measured mass flow for the use in the MPC and then to scale the determined mass flow setpoint back to the original mass flow size.

For an overview of the available measurements, table 3.2 lists the measured quantities and their usage in the coupled model. The available measurements and their usage in the coupled model are listed in Table 3.2.

3.5 Cloud Representation

In order to apply different cloud scenarios to the system, the previously described cloud definition by Geschonneck (2023), illustrated in Figure 2.8, is used. The main parameters of the cloud definition are the cloud shading, the cloud duration, its speed, and the start time of the cloud.

For the use in the controller, the cloud is represented by an array of DNI values. These values are defined for each heliostat group and for every time step in the considered simulation horizon. In this thesis, the transmissivity of the cloud is not considered. Thus, if a cloud shades a heliostat, it sets the corresponding DNI value to zero. The values of the unaffected heliostats correspond to the measured DNI value in the corresponding time step.

The shading parameter of the cloud affects the solar radiation that can be projected on the receiver. A shading parameter of 25 % would yield a solar radiation of 75 %. However, the shading parameter does not correspond to the percentage of shaded heliostat groups. Depending on the number of available heliostats and the distance to the receiver, each heliostat group affects the solar radiation differently. Thus, an algorithm determines how many heliostat groups have to be shaded to yield the desired radiation. To determine the radiation on the receiver the ray tracing tool `STRAL` is used.

However, the implementation of the algorithm only supports rectangular clouds that cover one side of the heliostat field, as depicted in Figure 3.8. Thus, the cloud affects all heliostats aligned in north-south direction. This leads to a further discretization of the heliostat field and implies that not every shading parameter can be represented by the algorithm.

Note that the algorithm also considers the cloud speed. The cloud moves in a straight line from south to north over the heliostat field. However, for long cloud durations and high cloud speeds, as applied in this thesis, the clouds behave like static shading events. The transition between the shaded and unshaded state is neglectable.

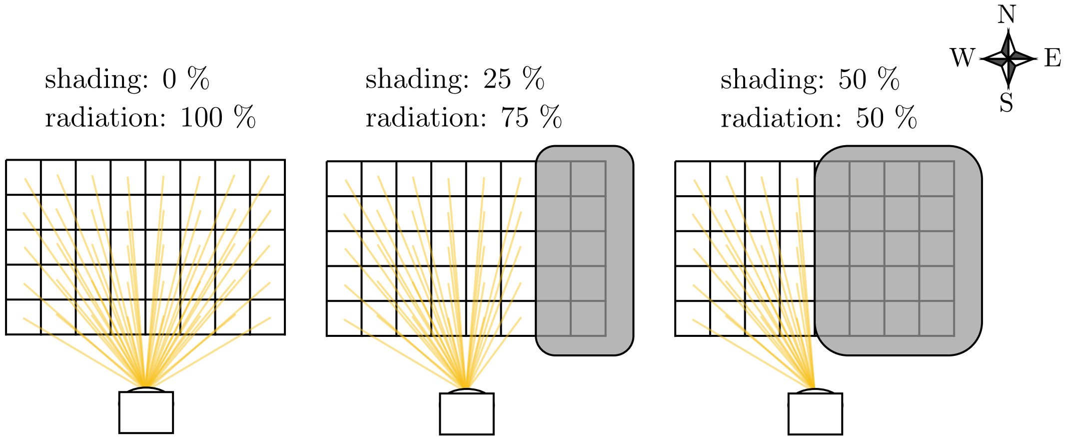

Figure 3.8: Cloud representation for different shading parameters.

4 Control Setup

The initial controller design and simulations made by Geschonneck (2023) were based on a physical model of the ceramic absorber cups and the valve analogy aim point strategy. For the simulations, a full state feedback without noise was assumed such that no state estimator was required.

In the further development by Zanger (2023), changes to the receiver model and the new aim point strategy were implemented, described in Chapter 3.2.1 and Chapter 3.1, respectively. Moreover, additions to the objective function of the MPC were made.

For the further enhancement of the model accuracy, a moving horizon estimator is designed to estimate the parameters of the polynomial receiver model. Finally, the controller parts are combined and implemented to suit the environment at the Solar Tower Jülich.

In the following sections, the applied adaptions on the MPC, the MHE design and the setup of the control at the experimental facility will be described. Additionally, the analysis of the heliostat movement times is presented, serving as a base for the control algorithm parametrization and its assessment of real-time capability.

4.1 Analysis of Heliostat Movement Times

As in the previous implementations, the control algorithm is supposed to be executed repeatedly with a time step of $t_{\text{step}} = 10\,\text{s}$. The analysis of a measurement series from May 2023 shows that the response time between the control command and the start of the heliostat movement averages to 6 s. The results are depicted in Figure 4.1. The delay is caused by two factors: the update time of incoming commands in the heliostat field operating system HeliOS (see Chapter 4.4) and the time needed to pass the commands from HeliOS to the corresponding heliostats in the field. However, the primary contributor to the delay is the command update frequency in HeliOS, which is set to 5 s by design.

The data also includes measurements of the duration for each heliostat to perform a defocus or refocus event. For a defocus, the heliostat aim point is set to the off-receiver aim point, which is a predefined point 50 m above and 50 m to the side of the receiver center, pointing into the sky. The refocus describes the inverse operation. Figure 4.1 depicts the mean times of the measured data for each heliostat, depending on the distance to the receiver. Note that the refocus and defocus durations include the response time.

From the measured data, the travel speed of the solar focal point induced by an heliostat can be estimated. This yields a mean travel speed of $3.6\,\text{m}\,\text{s}^{-1}$, depending on the distance between the heliostat and the receiver. The maximum possible travel distance for a solar focal point within the receiver surface can be defined by the diagonal of the receiver, which measures 6.8 m. With this, the mean maximum duration for aim point adjustments can be calculated to 1.9 s. Thus, the sum of the response delay and the actual aim point adjustment yields a total time of 7.9 s.

Consequently, considering the chosen time step of 10 s, the calculation of the control actions should be completed within less than 2.1 s to ensure that the control inputs are

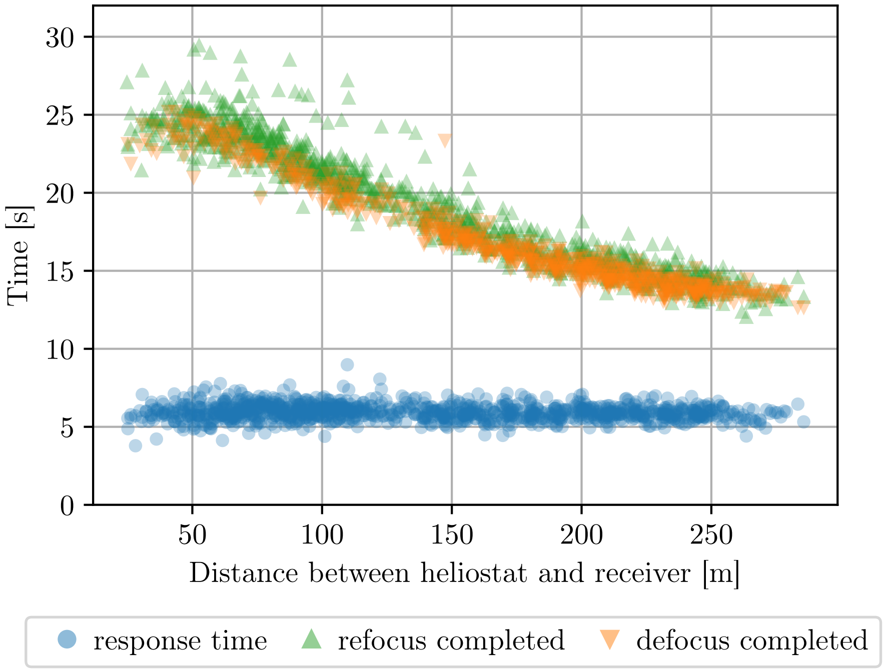

Figure 4.1: Heliostat mean times of the response delay and the durations of refocus and defocus events, dependent on the distance to the receiver.

fully applied before the start of the next iteration. Otherwise, the movement of the heliostats would have to be considered as a dynamical operation in the control loop.

However, this is only valid for the adjustments of aim points within the receiver surface. The figure also shows that the movements between the off-receiver aim point and the receiver can take up to 30 s, dependent on the distance between the heliostat and the receiver. This is especially relevant for the refocusing of heliostats as this control action might take up to 3 control iterations until it affects the flux density on the receiver surface. Thus, the controller should ideally limit the refocus and defocus events to a minimum by avoiding changes of κ_2.

4.2 Adaptions on the Model Predictive Controller

Due to the better accuracy of the polynomial model and the new aim point strategy, the model used in the MPC implementation has been adapted in several ways (Zanger, 2023). The objective function has been extended to not only account for the outlet temperature and input penalties but also incorporate a bound on the time derivatives $\dot{\boldsymbol{T}}_{\mathbf{abs,front}}$ and $\dot{\boldsymbol{T}}_{\mathbf{inlet,3}}$ as well as a measure to maximize the power output of the receiver (Zanger, 2023). The latter would ideally be implemented by maximizing the enthalpy of the outlet air $\dot{H}_{\text{out}} = \dot{m}_{\text{rec}} \cdot h_{\text{out}}$. However, to reduce the complexity of the objective function and to avoid the repeated calculation of the specific enthalpy, the term

$$\tilde{J}_2 = (T_{\text{out}} - T_{\text{return},3}) \cdot \dot{m}_{\text{rec}} \tag{4.1}$$

is maximized in the objective function instead.

Corresponding to the MPC formulation in Equations 2.3 - 2.7, the objective function for the MPC minimization problem gets defined as

$$J\left(\mathbf{x}_{\mathbf{u},k}, \mathbf{u}_k\right) = \sum_{i=1}^{4} J_i\left(\mathbf{x}_{\mathbf{u},k}, \mathbf{u}_k\right) \tag{4.2}$$

with

$$J_1(\mathbf{x}(t_n), \mathbf{u}(\cdot)) = \sum_{k=0}^{N-1} w_1 \cdot \left(T_{\text{out},k} - T_{\text{out,setpoint}}\right)^2 \tag{4.3}$$

$$J_2(\mathbf{x}(t_n), \mathbf{u}(\cdot)) = \sum_{k=0}^{N-1} w_2 \cdot \left(T_{\text{out},k} - T_{\text{return},3}\right) \cdot \dot{m}_{\text{rec},k} \tag{4.4}$$

$$J_3(\mathbf{x}(t_n), \mathbf{u}(\cdot)) = \sum_{k=0}^{N-1} \Delta\mathbf{u}_k^T \mathbf{R}\, \mathbf{u}_k \tag{4.5}$$

$$J_4(\mathbf{x}(t_n), \mathbf{u}(\cdot)) = \sum_{i=0}^{N-1} \boldsymbol{w}_{\boldsymbol{\xi}} \cdot \boldsymbol{\xi}_k. \tag{4.6}$$

Note that a terminal cost M is not implemented. The weighting factors and matrices are denoted as w_1, w_2, $\boldsymbol{w}_{\boldsymbol{\xi}}$ and $\mathbf{R}$. Additionally, $\boldsymbol{\xi}$ is a slack variable used to implement soft constraints. Soft constraints do not limit the feasible set, but increase the objective function by a penalty if the constraint is violated. Here, the bound on the surface temperature of the absorber cups $\boldsymbol{T}_{\textbf{abs,front}}$ as well as the newly added bounds on $\dot{\boldsymbol{T}}_{\textbf{abs,front}}$ and $\dot{\boldsymbol{T}}_{\textbf{inlet,3}}$ are implemented as soft constraints. The corresponding slack variables $\boldsymbol{\xi} = [\xi_1, \xi_2, \xi_3]^T$ are defined as

$$\xi_1 = \begin{cases} 0 & \text{for } T_{\text{abs,front}} \leq 1255.75\,\mathrm{K} \\ T_{\text{abs,front}} - 1255.75\,\mathrm{K} & \text{for } T_{\text{abs,front}} > 1255.75\,\mathrm{K} \end{cases} \tag{4.7}$$

$$\xi_2 = \begin{cases} 0 & \text{for } \dot{T}_{\text{abs,front}} \leq 1.5\,\mathrm{K\,s^{-1}} \\ \dot{T}_{\text{abs,front}} - 1.5\,\mathrm{K\,s^{-1}} & \text{for } \dot{T}_{\text{abs,front}} > 1.5\,\mathrm{K\,s^{-1}} \end{cases} \tag{4.8}$$

$$\xi_3 = \begin{cases} 0 & \text{for } \dot{T}_{\text{inlet},3} \leq 1.5\,\mathrm{K\,s^{-1}} \\ \dot{T}_{\text{inlet},3} - 1.5\,\mathrm{K\,s^{-1}} & \text{for } \dot{T}_{\text{inlet},3} > 1.5\,\mathrm{K\,s^{-1}}. \end{cases} \tag{4.9}$$

Hence, if the surface temperature in any cup exceeds 1255.75 K or an increase in the receiver temperatures of more than $1.5\,\mathrm{K\,s^{-1}}$ is expected, a cost is added to the objective function. The addition of the soft constraints ensures the safe operation within the operating limits of the receiver. In the process control system (see Chapter 4.4), these limits are defined as

$$\dot{T}_{\text{abs,front}} \leq 3\,\mathrm{K\,s^{-1}}, \tag{4.10}$$

$$T_{\text{abs,front}} \leq 1275.75\,\mathrm{K}. \tag{4.11}$$

If they are violated, the process control system triggers a safety defocus event to prevent damage to the receiver. The implemented soft constraints are intentionally chosen with an additional safety margin. This way, the safety defocus can be avoided even when the soft constraints are exceeded or the model is not accurate enough to detect the violation.

The addition of J_2 compared to the previous implementation, helps to avoid a solution where the outlet temperature meets the set point perfectly by reducing the mass flow instead of increasing the solar radiation on the receiver. This would result in a lower power output of the receiver and thus a lower efficiency of the system, which does not align with the control goal.

The weighting factors and matrices are tuning parameters for the controller. For the initial choice in the simulations and experiments, the values

$$w_1 = 5 \tag{4.12}$$

$$w_2 = 3 \tag{4.13}$$

$$\boldsymbol{w_\xi} = \begin{bmatrix} 1 \cdot 10^4 \\ 1 \cdot 10^4 \\ 1 \cdot 10^4 \end{bmatrix} \tag{4.14}$$

$$\mathbf{R} = \begin{bmatrix} 0.1 & 0 & 0 \\ 0 & 5 \cdot 10^4 & 0 \\ 0 & 0 & 1 \end{bmatrix} \tag{4.15}$$

were used, considering the control input change $\Delta\mathbf{u} = [\Delta\kappa_1, \Delta\kappa_2, \Delta\dot{m}_{\text{setpoint}}]^T$.

With the higher weight for the control input κ_2 compared to κ_1, the controller is encouraged to adapt the focus of the heliostats by adjusting κ_1 prior to defocusing heliostats by lowering κ_2. As described earlier, this is a favorable behavior because the defocusing and especially the refocusing of heliostats take much longer compared to merely adjusting the aim point within the receiver surface. Additionally, it is preferable to avoid unnecessary defocusing and refocusing events to reduce the wear of the heliostat actuators.

Note that the above-stated weighting values have been chosen empirically during a first set of experiments (Zanger, 2023) and might not be optimal yet.

Apart from the adaptions on the objective function, the hard constraints on the aim point control inputs were implemented as described in Chapter 3.1. However, if not all heliostats in the field are operational, the upper bound on κ_2 gets adapted. It is set such that it aligns with the percentage of heliostats that are reported to be available by HeliOS during the initialization of the controller. Furthermore, the constraint on the mass flow set point is set to $\dot{m}_{\text{setpoint}} \in [2.93, 7.5\,\text{kg}\,\text{s}^{-1}]$, to limit the range for the first set of experiments (Zanger, 2023). The real operational range of the fan goes up to $11.7\,\text{kg}\,\text{s}^{-1}$. In the implementation, the bounds of the mass flow are scaled by the mass flow ratio $\mu_{\dot{m}}$ to account for the reduced model.

For the prediction horizon of the MPC, $N_{\text{MPC}} = 6$ is used, resulting in a prediction time of 1 min.

4.3 Estimator Design

Using the polynomial model for the receiver, the states $\mathbf{x} = [\boldsymbol{T}_{\mathbf{abs,front}}, \boldsymbol{T}_{\mathbf{inlet,3}}, \dot{m}_{\text{rec}}, \ddot{m}_{\text{rec}}]^T$ are known either by measurement or derivation from another state. Thus, no state estimation is necessary. However, the use of an estimator can still be beneficial if measurements are effected by noise. Furthermore, it can be used to estimate uncertain parameters of a model.

In the case of the polynomial model, an estimator is supposed to adapt the parameters p_i for $i \in \{0, \ldots, 9\}$ of the model to account for inaccuracies in the polynomial approximation stated in Equations 3.14 - 3.17. As described in Chapter 2.2.2, the moving horizon estimator is a suitable choice for both applications and can handle nonlinear systems as well as constraints. Additionally, the used do-mpc toolbox provides an MHE implementation, which can reuse the model or model parts implemented for the MPC. However, a drawback of an MHE is the higher computational effort compared to a Kalman Filters, as it requires the solution of an optimization problem in each iteration. Thus, it has to be investigated if the use of the MHE and the chosen implementation are feasible for the control of the solar tower system with regards to the applied sampling time.

4.3.1 Moving Horizon Estimator Setup

The MHE can be set up in two different ways. It can either apply the same model setup as the MPC, combining the individual absorber cup models into one model. Alternatively, the MHE can be implemented using a separate model for each of the 30 representative cups (later referred to as Single Cup MHE).

The first approach has the advantage of a lower computational effort since only one optimization problem has to be solved. However, using the do-mpc toolbox, only the second approach is feasible, as do-mpc does not support the implementation of multi-dimensional parameters. This would be required for the combined model with 30 cups.

For the implementation of the Single Cup MHE, the do-mpc MHE functionality had to be embedded into a loop over the 30 representative cups, as illustrated in Figure 4.2. Since the MHE is dependent on the knowledge of the system states of N_{MHE} steps in the past, a measurement history is created and updated in each controller iteration. For each cup, the corresponding history of the model variables and measurements is set before the MHE optimization problem gets solved. Finally, the resulting parameter array $\boldsymbol{p}$ consisting of the estimated parameters for each cup $\boldsymbol{p}_{\text{cup}}$ is passed to the MPC, where the model is updated correspondingly.

The do-mpc implementation of the MHE optimization problem align with the description in Equations 2.11 - 2.14 and is parametrized using

$$\mathbf{P}_{\mathbf{x}} = 10^3 \cdot \mathbf{I}_4 \tag{4.16}$$

$$\mathbf{P}_{\mathbf{p}} = 10 \cdot \mathbf{I}_{10} \tag{4.17}$$

$$\mathbf{P}_{\mathbf{v}} = 10^2 \cdot \mathbf{I}_3 \tag{4.18}$$

$$\mathbf{P}_{\mathbf{w}} = 0 \tag{4.19}$$

$$N_{\text{MHE}} = 12, \tag{4.20}$$

with $\mathbf{I}_n$ denoting an $n \times n$ identity matrix. The horizon length follows the performance analysis presented in Chapter 4.3.2. In general, a higher horizon length results in a more

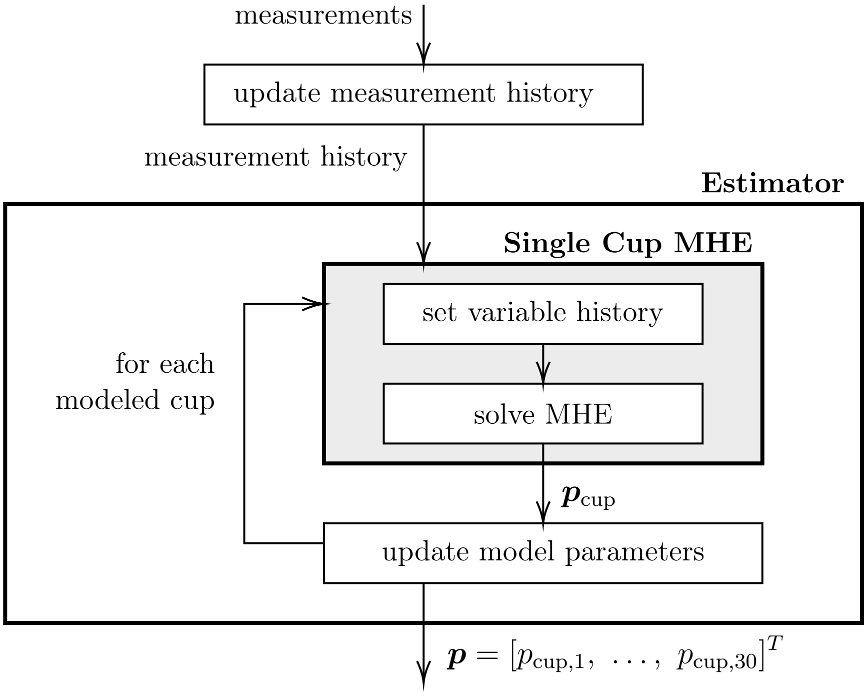

Figure 4.2: Implementation of the MHE parameter estimation for multiple cups.

accurate estimation, but also increases the computational effort.

As in the MPC, the specific values of the weighting factors are based on empirical values. The choice to set $\mathbf{P_x}, \mathbf{P_v} \gg \mathbf{P_p}$ was made to adapt the model closely to the measured variables, allowing the estimated parameters to change in each iteration. However, this parametrization can lead to an overfitting of the model to the measurements and rapidly changing parameters. With the choice of $\mathbf{P_p} \neq 0$, the risk of overfitting is reduced as parameter changes are penalized. Additionally, the longer the horizon length the less rapid the parameter changes are.

Note that in the implementation, all values of the variables and parameters are scaled to a similar order of magnitude to improve the numerical stability of the optimization problem.

The set of constraints for the MHE optimization problem only consists of inequality constraints, forming the bounds for the estimated parameters. To ensure the correct model behavior, suitable bounds on the estimated parameters are crucial. For example, a positive value for the constant c_2 in Equation 3.10 indicates that the steady-state of the surface temperature $T_{\text{abs,front,ss}}$ increases with higher solar flux values. However, if the corresponding parameter p_2 would alter the expression $(c_2 + p_2)$ in Equation 3.16 to a negative value, the effect of the solar flux on the surface temperature would be inverted. To prevent this, the bounds for the parameters influencing the steady-state values of the polynomial model are set to

$$|p_i| < \mu_{bounds} \cdot c_i \quad \text{for } i \in \{1, \dots, 4\} \cup \{6, \dots, 9\}, \tag{4.21}$$

with the design factor $\mu_{bounds} \in [0, 1]$. For simplicity, the bounds are chosen to be symmetric. The value of μ_{bounds} determines the extent to which the parameter can influence the corresponding fitted constant c_i. In the simulations and experiments a value of $\mu_{bounds} = 0.3$ is used to limit the influence of the parameters. The bounds for the parameters p_0 and p_5, which define the dynamic behavior of the model, result directly from the fitting process of the polynomial model (Zanger, 2023).

4.3.2 Performance Analysis

To investigate the performance of the estimator using the Single Cup MHE implementation, simulations are conducted on a Windows 10 (64 bit) system equipped with an 11th Gen Intel(R) Core(TM) i7-1185G7 @ 3.00 GHz CPU using 4 cores and 16 GB of RAM.

First, the estimator process times, dependent on the horizon length N_{MHE}, are analyzed. Table 4.1 shows the resulting mean and maximum computation times for

(i) solving only the optimization problem for one cup,

(ii) running the Single Cup MHE for one cup, including the mapping and setting of the relevant measurement histories and

(iii) running the complete estimation for all cups.

Table 4.1: Process times for the parameter estimation for different MHE horizon lengths.

N_{MHE}		(i): Solver	(ii): 1 Cup	(iii): 30 Cups
6	(mean)	0.013 s	0.028 s	**0.835 s**
	(max)	0.030 s	0.126 s	1.008 s
12	(mean)	0.021 s	0.046 s	**1.387 s**
	(max)	0.045 s	0.137 s	1.706 s
20	(mean)	0.027 s	0.066 s	**1.970 s**
	(max)	0.072 s	0.166 s	2.527 s

As expected, the computation time increases with a higher horizon length but does not exceed 2 s for the tested values. Furthermore, we can observe, that the solving of the optimization problem (i) accounts for less than 50 % of the total computation time for one cup. The remaining time is used for the required operations to set the measurement histories to the corresponding `do-mpc` quantities. This overhead time has already been reduced by using more efficient functions and data structures in the implementation.

Based on the results, the horizon length is chosen to be $N_{\text{MHE}} = 12$, as it shows a good trade-off between accuracy and computational effort. However, to ensure that the mean time of 1.3866 s of the estimator is acceptable within the control loop, the performance of the complete control algorithm was measured as well and presented in Table 4.2.

Table 4.2: Process times for the control algorithm and its subparts for $N_{\text{MHE}} = 12$ and $N_{\text{MPC}} = 6$.

	Mean process time	Maximum process time
Estimator (MHE)	1.387 s	1.706 s
MPC	0.131 s	0.175 s
Complete control algorithm	**1.590 s**	**1.930 s**

We see, that the MHE accounts for more than 90 % of the total process time of the control algorithm. The MPC is more than 1 s faster, which is due to the combined receiver model used in the MPC implementation. This way, the mapping of the incoming measurements to the corresponding do-mpc variables is only performed once for the complete model instead of 30 times for each individually modeled cup.

However, the duration for the complete control algorithm does not exceed 2 s. Since this aligns with the design goal formulated in Chapter 4.1, this implementation will be used for the simulations and experiments. However, it might become necessary to adapt the MHE horizon length or the estimator implementation in case the real-time capability cannot be ensured. Nevertheless, as the complete control algorithm only accounts for less than 20 % of the step time, improvements on it would not have a significant impact on the duration of the control loop.

4.4 Integration into the Solar Tower Environment

For the experimental validation, the controller needs to be connected to the real system environment at the solar plant in Jülich. Additionally, to test the performance of the control under the influence of cloud passages, a cloud mock-up was implemented that defocuses heliostats as if covered by a cloud. Figure 4.3 shows the interaction between the different components of the experimental setup, which will be explained in the following. Additionally, the implementation of a flux density mock-up, used as compensation for a missing solar flux measurement, will be described.

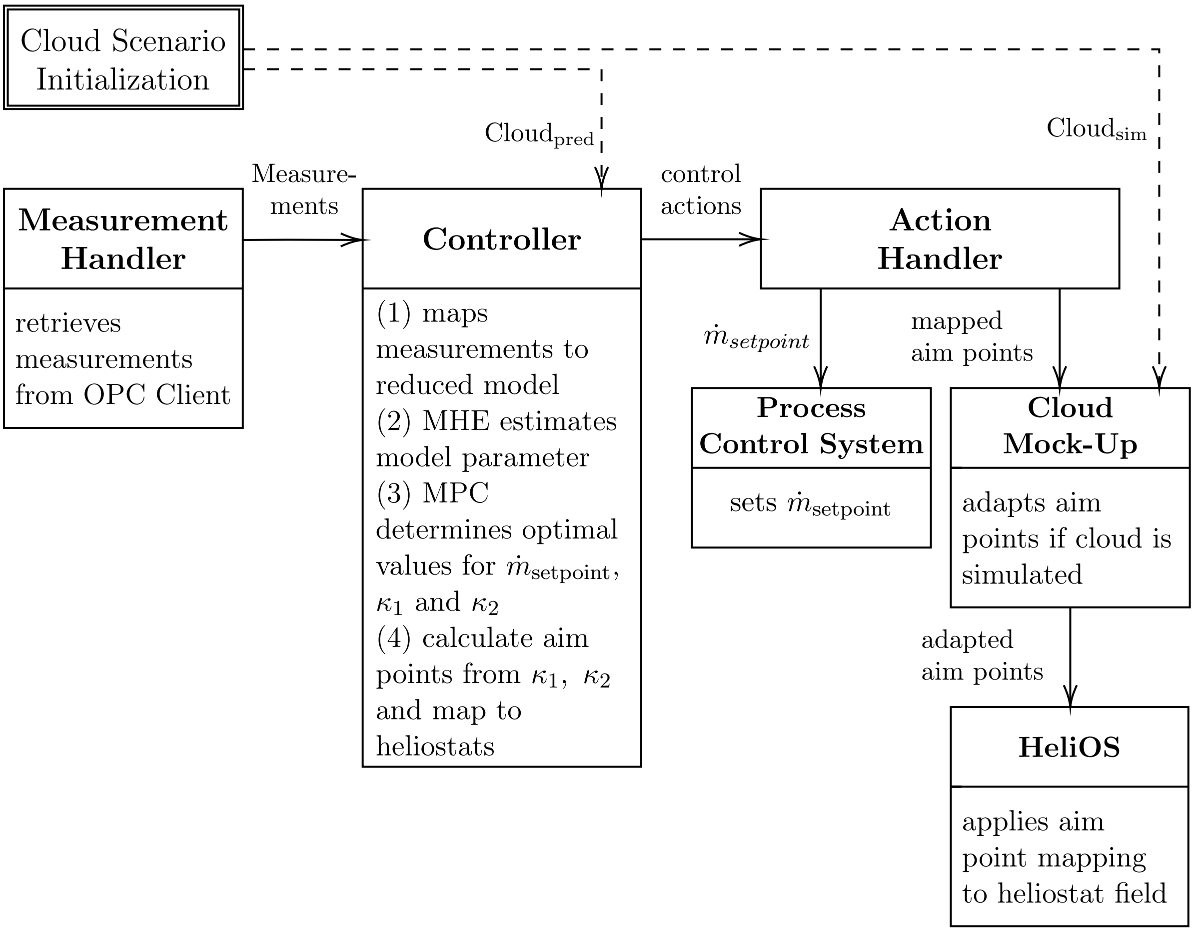

Figure 4.3: Interaction between the subsystems within one control iteration.

Measurement Handler The measurement handler retrieves the measurements from the different sensors in the system, mostly from the process control system via an Open Platform Communications (OPC). Some data, for example the information about the currently available heliostats, is also provided directly by the heliostat operating system HeliOS, described below.

Action Handler The action handler receives the control commands from the control unit and transmits them to the corresponding client. The set point for the mass flow is passed directly to the fan controller via an OPC client. The aim points and their mapping to the corresponding heliostats are not applied directly to the heliostat field but passed through the cloud mock-up to simulate the passing of a predefined cloud. A more detailed description of the cloud mock-up is stated below.

Process Control System The process control system acts as higher level management system for the solar tower and consists of several PLC (Programmable Logic Control) units. It applies the corresponding control command to the fan, where a sublevel controller adjusts the fan speed and its valve to meet the mass flow set point. It also processes the signals from the measurement devices in the tower and transmits them through an OPC Client. Furthermore, it is responsible for the safety of the system. If it detects an unsafe system state, such as too high receiver surface temperatures, it triggers the defocus of the heliostat field to prevent damage to the receiver.

Cloud Mock-Up The cloud mock-up is initialized with the cloud $\text{Cloud}_{\text{sim}}$. As described in Chapter 3.5, clouds are represented as an array of DNI values for each group of heliostats. However, for the cloud mock-up, the array only contains binary values, indicating if the heliostat group is shaded by the cloud or not. For the shaded heliostat groups, the cloud mock-up changes the associated aim points calculated by the controller to the predefined off-receiver aim point. This replicates the effect of a cloud coverage of the heliostats as they will defocus and not project any radiation onto the receiver anymore. The adapted aim points are passed to HeliOS to be applied to the heliostat field.

HeliOS The Heliostat Operating System (HeliOS) was developed by the DLR as a universal, platform-independent control system for different types of heliostats and receivers. It transmits the control commands to the heliostat field actuators and receives the position feedback. Furthermore, it allows the operator to monitor the heliostat field data and to control the heliostats manually.

Flux Density Mock-Up The flux density mock-up, which is not depicted in Figure 4.3, is an additional component of the experimental setup. It is used to simulate the flux density measurement at the receiver, in the case that the corresponding measurement device is not available yet. Similar to the flux density approximation used in the model, it is based on the ray tracing tool STRAL. However, to yield more precise results suitable to simulate a measurement with, STRAL is used directly to calculate the flux density at the receiver instead of approximating its results by a polynomial.

5 Simulations

Due to the described adaptions of the controller, a comparison between the simulations from Geschonneck (2023) and measured data from experiments on the real system would not be valid anymore. Therefore, the simulations for different cloud scenarios and uncertainties in the predictions are repeated for the new controller setup. Additionally, it will be investigated if the parameter estimation by the moving horizon estimator can improve the accuracy of the model and thus the performance of the controller.

5.1 Setup

For the simulations, the control system is connected with a simulator using the corresponding `do-mpc` functionality. The simulator is initialized with the same model as the MPC. However, in the polynomial receiver model it only uses the fitted constants c_i as they assumed to be optimal.

The control setup varies for the different simulations. In a first set of simulations, the controller will be tested without the MHE. Later, the estimator as described in Chapter 4.3 is added to the control setup, estimating the parameters p_i of the polynomial receiver model. It will be investigated if the parameter estimation can improve the performance and robustness of the controller. In order to test the influence of inaccuracies in the fitting of the polynomial model constants, one set of simulations will use an adapted MPC model where the parameters p_i are initialized with an inaccurate parameter set.

For each of the control setups, different cloud scenarios are tested based on the cloud definitions made by Geschonneck (2023). However, only the shading parameters differ between the scenarios. The duration of the cloud passage with 120 s and the cloud speed of $30\,\mathrm{m\,s^{-1}}$ remain constant for every defined cloud. The ramp time is set to 20 s for all clouds. Similar to the described setup for the experiments, two clouds can be defined. The cloud $\mathrm{Cloud}_{\mathrm{sim}}$ is used by the simulator representing the actual drop of radiation the system is exposed to. The cloud definition of $\mathrm{Cloud}_{\mathrm{pred}}$ on the other hand is used to simulate the prediction of the clouds and is applied in the MPC.

As described in Chapter 3.5, not every cloud shading parameter can be represented. The discretization of the feasible shading parameters depends on the amount and distribution of available heliostats. For the simulations, a set of 1388 heliostats distributed over the field is used. This list of heliostats is based on recent information about the currently operational heliostats at the Solar Tower Jülich. Based on the available heliostats and resulting resolution of the algorithm, the shading parameters of 25 %, 50 % and 70 % were chosen for the simulations. These values represent a wide range of cloud scenarios, such that the control performance can be evaluated for both challenging and less challenging cloud conditions.

For the exact predictions all three shading parameters are tested with $\mathrm{Cloud}_{\mathrm{sim}} = \mathrm{Cloud}_{\mathrm{pred}}$. The simulations with inaccurate shading predictions are performed for a shading parameter of 50 % for $\mathrm{Cloud}_{\mathrm{sim}}$ and 25 % and 70 % for $\mathrm{Cloud}_{\mathrm{pred}}$. This way, both an underestimation as well as an overestimation of the shading can be evaluated.

If not stated differently, the parametrization and bounds of the MPC and MHE as defined in Chapter 4 are applied. For the initialization of the system, the steady-state values of the states and inputs as listed in Table 5.1 are used. Note that the steady-state value of the surface temperature $T_{\text{abs,front}}$ is lower than the outlet air temperature $T_{\text{inlet,3}}$ of the absorber cup. As mentioned in Chapter 2.1.3, this behavior results from the open volumetric structure of the receiver. The air flow through the receiver cools the absorber surface while being heating up.

In the planned experiments at the solar tower, a sufficient margin to the maximum allowed surface temperature of the absorber cups ($T_{\text{abs,front,max}} = 1275.75\,\text{K}$) is desired to ensure a safe operation of the system. Moreover, with only 1388 of the 2153 heliostats available, the amount of solar radiation that can be applied to the receiver is reduced. Thus, the set point for the outlet temperature $T_{\text{out,setpoint}}$ is chosen lower than in the simulations by Geschonneck (2023) to allow for a more realistic comparison with the experimental data. However, this also leads to a more relaxed control problem, as it can be assumed to be easier to find a feasible solution for set points farther away from the bound on $T_{\text{abs,front}}$.

Table 5.1: Steady-state values for the system initialization.

Variable type	Variable name	Value
reference r	$T_{\text{out,setpoint}}$	$750\,\text{K}$
states x	$T_{\text{abs,front}}$	$810\,\text{K}$
	$T_{\text{inlet,3}}$	$820\,\text{K}$
	$\dot{m}_{\text{rec}}$	$7.5\,\text{kg}\,\text{s}^{-1}$
	$\ddot{m}_{\text{rec}}$	$0\,\text{kg}\,\text{s}^{-2}$
inputs u	$\dot{m}_{\text{setpoint}}$	$7.5\,\text{kg}\,\text{s}^{-1}$
	κ_1	0.64
	κ_2	0.52

Note that the set point for the mass flow is initialized with the value for the upper bound as defined in Chapter 4.2. Due to the additional term in the objective function, the controller will always maximize the mass flow to increase the enthalpy of the outlet air flow. Thus, if enough solar radiation is available, the mass flow will be at its maximum value in the steady-state.

All simulations will be plotted showing the outlet temperature T_{out} and the control inputs κ_1, κ_2 and $\dot{m}_{\text{setpoint}}$. For simplicity, the simulated mass flow value will not be plotted separately. It is similar to the trajectory of the set point and mainly differs in a time shift corresponding to the time constant in the fan model. The applied cloud $\text{Cloud}_{\text{sim}}$ will be represented by the resulting drop in the solar radiation. The surface temperature $T_{\text{abs,front}}$ will only be plotted for one chosen absorber cup in the receiver center (Cup 15, as highlighted in Figure 3.7). The central absorber cups usually yield the highest temperatures, as they receive most of the radiation. Thus, they are a valid choice to evaluate the margin to the maximum allowed temperature.

Additionally, the relative enthalpy flows as a measure for the exergy input to the downstream process are depicted. The relative enthalpy flows are calculated as

$$\dot{H}_{\text{out}} = \dot{m}_{\text{rec}} \cdot (h_{\text{out}} - h_{\text{amb}}). \tag{5.1}$$

To ensure the steady-state of the system in the beginning, all simulations started 100 s prior to the simulation time depicted in the plots. For the evaluation of the controller performances, the Root Mean Square Error (RMSE) of the outlet temperature T_{out} to its set point is used. Additionally, the RMSE of the enthalpy flow $\dot{H}_{\text{out}}$ compared to its initial value of $3.5\,\text{MJ}\,\text{s}^{-1}$ is calculated.

All simulations are conducted on the same system as the performance analysis, specified in Chapter 4.3.2.

5.2 Simulations without Parameter Estimation

5.2.1 Cloud Scenarios with Exact Cloud Prediction

In the first set of simulations, the control performance without the use of the MHE and with exact cloud predictions is evaluated. Similar to Geschonneck (2023), simulations for the system with cloud disturbances but without any control actions are performed first. These reference scenarios can be used as base cases to evaluate the performance of the controller. The results of the reference scenarios are depicted in Figure 5.1 as dotted lines. It shows that the outlet temperature as well as the enthalpy flow drop significantly during the cloud passage. For a cloud scenario with a shading of 50 %, the temperature changes by more than 100 K. The enthalpy flow reaches a minimum of $2.7\,\text{MJ}\,\text{s}^{-1}$. Table 5.2 summarizes the RMSE values of the outlet temperature and the enthalpy flow for the different cloud shading parameters. Furthermore, for all scenarios, it takes over 150 s to recover from the cloud passage and reach the steady-state again.

Table 5.2: RMSE values of T_{out} and $\dot{H}_{\text{out}}$ for the reference scenarios without control actions.

Shading $\text{Cloud}_{\text{sim}}$	$\text{Cloud}_{\text{pred}}$	RMSE T_{out}	$\dot{H}_{\text{out}}$
25 %	–	29.2 K	$234.2\,\text{kJ}\,\text{s}^{-1}$
50 %	–	59.3 K	$519.8\,\text{kJ}\,\text{s}^{-1}$
70 %	–	79.3 K	$708.8\,\text{kJ}\,\text{s}^{-1}$

In a second step, the simulations are repeated using the model predictive controller as defined in Chapter 4.2 without any parameter estimation by the MHE. The results are depicted in Figure 5.1 as well. For all scenarios, the controller has the exact knowledge of the cloud passage, with $\text{Cloud}_{\text{pred}} = \text{Cloud}_{\text{sim}}$. We see, that for all three cases, the controller reacts with adapted control inputs before the cloud passage starts at $t = 50\,\text{s}$. Due to the knowledge of the upcoming disturbance, it starts raising the control inputs κ_1 and κ_2 to increase the power projected on the receiver and thus compensate for the upcoming temperature drop. According to the prediction horizon, this predictive behavior starts 12 s prior to the start of the cloud.

For a shading of 25 % and 50 % the controller is able to compensate the cloud passage significantly, mostly by adjusting the aim point control inputs. The outlet temperature T_{out} is kept within a range of ±8 K to the set point for a shading of 25 % and ±20 K for a shading of 50 %. The enthalpy flow is only slightly reduced during the cloud passage.

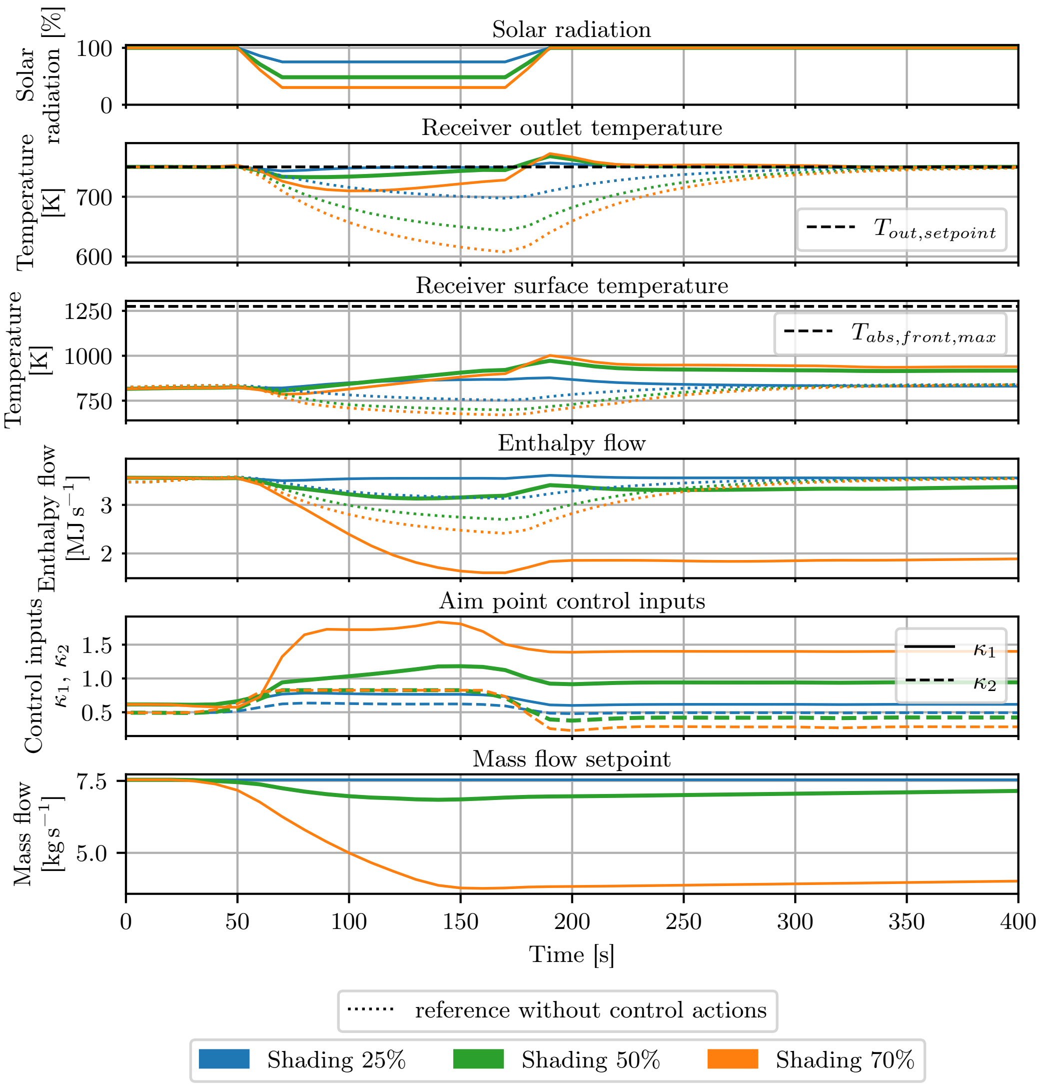

Figure 5.1: System behavior and control actions for different cloud shading parameters and exact predictions.

Additionally, the controller compensates the temperature drop within less than 50 s after the cloud passage.

However, for a shading of 70 % the outlet temperature and enthalpy flows drop significantly. The enthalpy flow gets even lower than in the reference scenario and reaches a RMSE value of 1.1 MJ s^{-1}. The controller focuses on keeping the outlet temperature close to the set point, as this is the primary objective. It is also noticeable, that even after the cloud passage, the controller is not able to steer the system back to the initial states. Instead, the mass flow is reduced and the input values κ_1 and κ_2 are lower compared to their initial values. This results in less power projected on the receiver, leading to an enthalpy flow 1.5 MJ s^{-1} lower than its initial value. This behavior was aimed to avoid by the addition of the term J_2 to the objective function stated in Equation 4.4. Based on these results we can assume that the chosen weighting factor for the added term is not sufficient yet. Thus, for all following simulations the weighting factor w_2 is increased from $w_2 = 3$ to $w_2 = 50$.

Figure 5.2 shows the results for the adapted controller design. We immediately see the effect of the increased weighting factor. Even though the behaviors during the cloud passage are very similar, the controller now steers the system back to the initial enthalpy flow value within the depicted time frame after the cloud has passed. The resulting RMSE values are listed in Table 5.3, including their proportional changes compared to the uncontrolled reference scenarios.

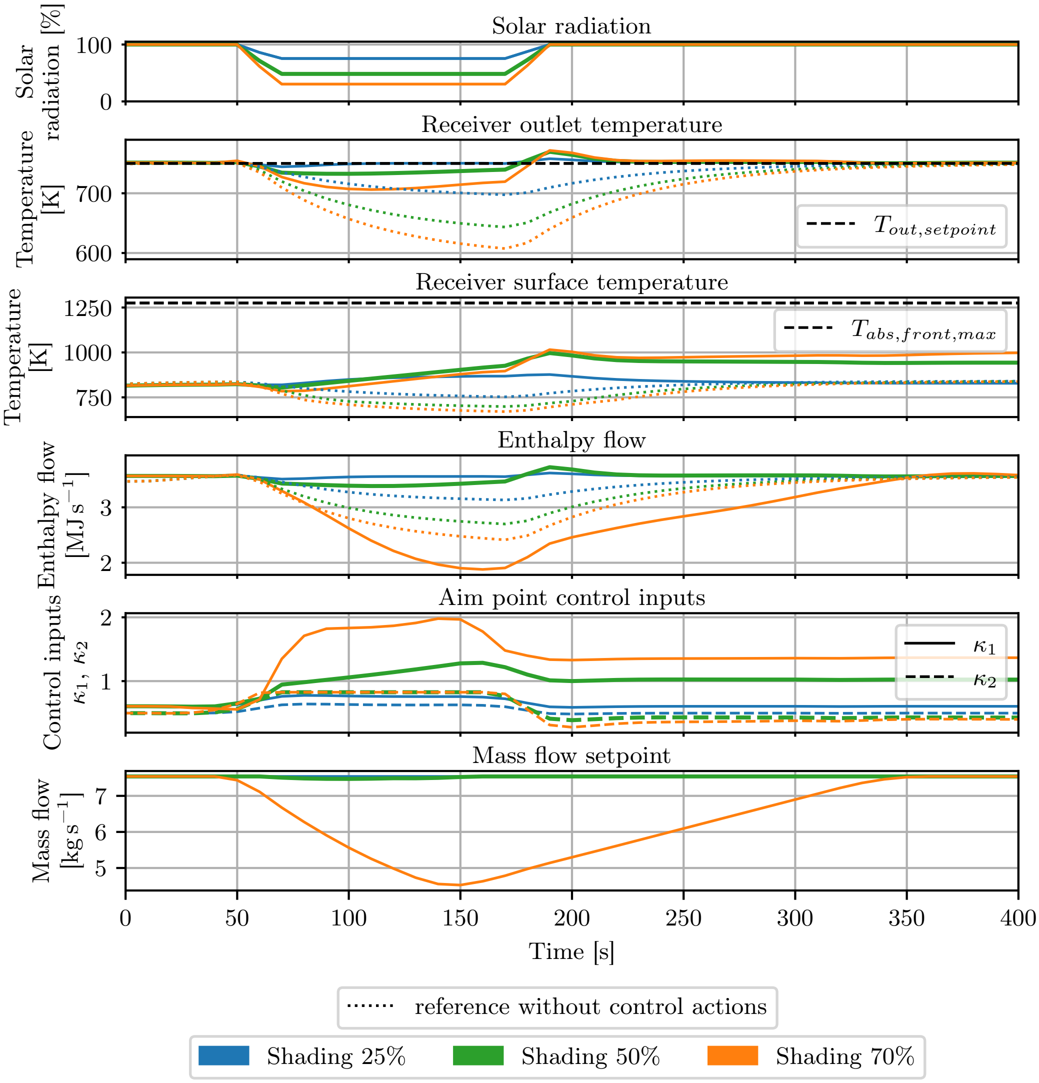

Figure 5.2: System behavior and control actions for different cloud shading parameters and exact predictions with the adapted weighting factor $w_2 = 50$.

Even though the change in the weighting factor enabled the controller to improve the RMSE value of the enthalpy flow, it is still noticeable that different optimal solutions compared to the initial steady-state values are found. Since the objective function value is the same for the initial and the new steady-state, this shows the existence of multiple global optimal solutions for the optimization problem. The solutions differ in the ratio between the applied control inputs κ_1 and κ_2.

As described earlier, due to the long distance between the off-receiver aim point and the receiver, the controller is encouraged to adjust the aim points within the receiver surface

Table 5.3: RMSE values of T_{out} and $\dot{H}_{\mathrm{out}}$ for cloud scenarios with exact predictions in comparison to the reference scenarios without control actions.

Shading		RMSE		Δ RMSE	
Cloud$_{\mathrm{sim}}$	Cloud$_{\mathrm{pred}}$	T_{out}	$\dot{H}_{\mathrm{out}}$	T_{out}	$\dot{H}_{\mathrm{out}}$
25 %	25 %	2.7 K	70.7 kJ s^{-1}	−90.7 %	−69.8 %
50 %	50 %	10.5 K	106.4 kJ s^{-1}	−82.3 %	−79.5 %
70 %	70 %	23.4 K	1105.0 kJ s^{-1}	−70.5 %	+55.9 %

by changing κ_1 before applying changes to κ_2. To achieve this, the weighting factor for adaptions in κ_1 has been more than 10^5 times higher than for κ_2 (see Chapter 4.2). However, we still observe a decrease of more than 50 % in κ_2 when the cloud passes. Thus, a further adaption on the weighting factors might be necessary and should be further investigated in the experiments on the real system.

5.2.2 Cloud Scenarios with Inaccurate Cloud Prediction

In order to investigate the robustness of the controller without the MHE, the simulations are repeated with uncertainties in the cloud predictions. This is tested by using different cloud shading parameters for the predicted cloud Cloud$_{\mathrm{pred}}$ compared to the simulated cloud Cloud$_{\mathrm{sim}}$. Results for a simulated cloud with a shading of 50 % and predictions with shadings of 25 % and 70 % are depicted in Figure 5.3. For comparison, the result for the exact prediction with Cloud$_{\mathrm{pred}}$ = Cloud$_{\mathrm{sim}}$ is shown as well.

As expected, for both the underestimation and overestimation of the shading parameter, the controller is performing worse than for the exact prediction.

For the estimated shading parameter of 70 %, the controller reacts with significant changes in the control inputs compared to the exact prediction. The mass flow is reduced by more than 1.5 kg s^{-1} and the input values κ_1 almost reaches its upper bound. The low applied mass flow leads to a drop in the enthalpy flow. Furthermore, the strong focusing on the receiver center results in a rising surface temperature of the depicted absorber cup and an increase in the outlet temperature by 35 K compared to the set point. Similar to the corresponding cloud scenario with an exact prediction (Figure 5.2), the steady-state values of κ_1 and κ_2 show significant changes compared to their initial values. Additionally, the difference between κ_1 and κ_2 has increased: the value for κ_1 rises whereas the value of κ_2 is lowered.

The controller with the underestimated shading parameter on the other hand shows a different behavior. Concerning the outlet temperature, a maximal deviation from the set point of over −70 K can be observed. This results in a drop of the enthalpy flow by 0.5 MJ s^{-1} compared to the initial value. Furthermore, the underestimation leads to very limited control actions, compared to the exact prediction.

In both cases, the controller shows limited capability to handle the uncertainties in the cloud prediction. Table 5.4 summarizes the relevant RMSE values for the outlet temperatures and the enthalpy flows for the different scenarios. The results highlight the importance of accurate cloud predictions for the applied controller design.

Table 5.4: RMSE values of T_{out} and $\dot{H}_{\text{out}}$ for cloud scenarios with a shading of 50 % and varying cloud shading predictions.

Shading		RMSE	
$\text{Cloud}_{\text{sim}}$	$\text{Cloud}_{\text{pred}}$	T_{out}	$\dot{H}_{\text{out}}$
50 %	25 %	36.1 K	$309.0\,\text{kJ}\,\text{s}^{-1}$
50 %	50 %	10.5 K	$106.4\,\text{kJ}\,\text{s}^{-1}$
50 %	70 %	16.4 K	$374.8\,\text{kJ}\,\text{s}^{-1}$

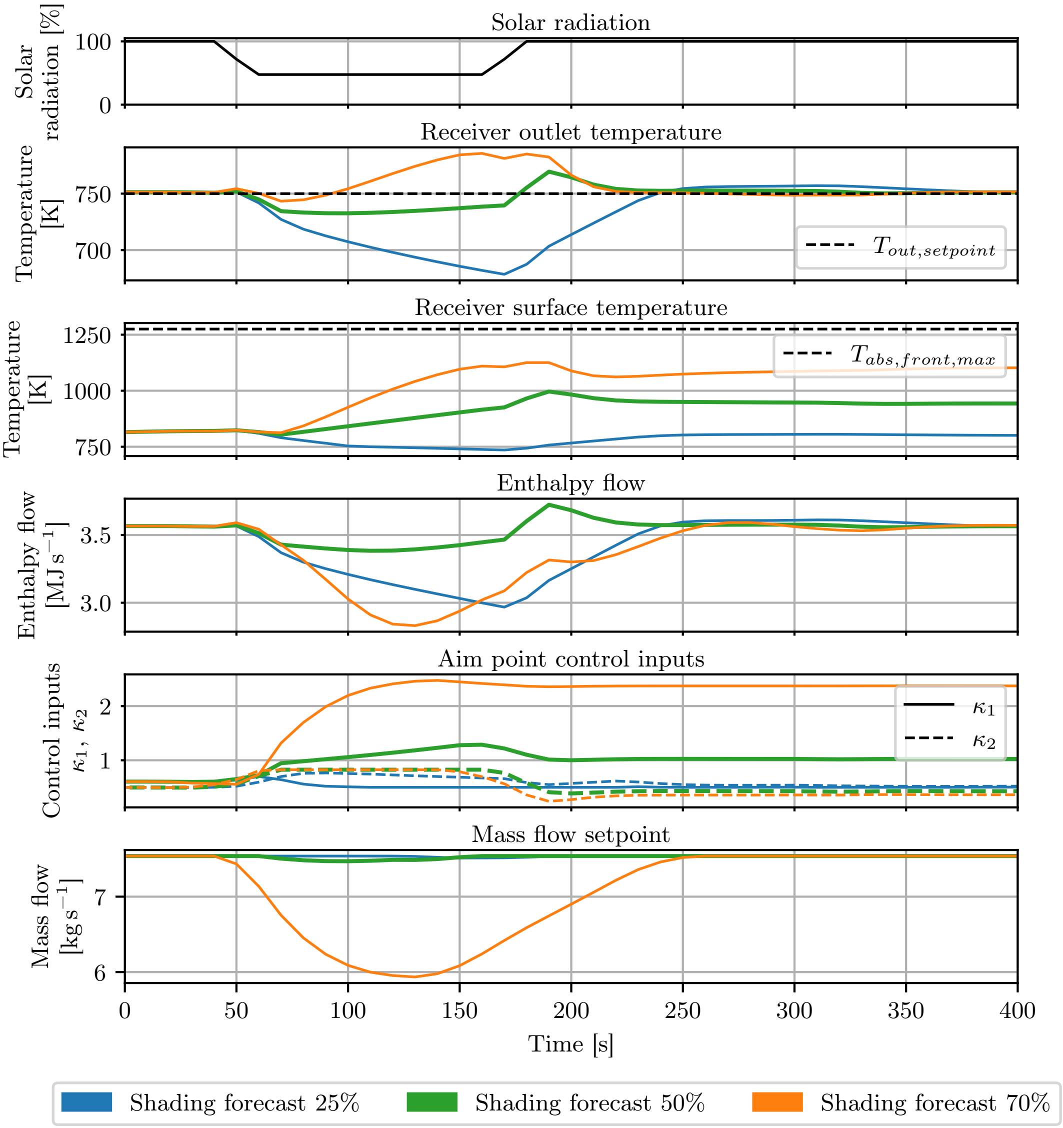

Figure 5.3: System behavior and control actions for a cloud shading of 50 % and predicted shadings of 25 %, 50 % and 70 %.

5.3 Simulations with Parameter Estimation

In the second set of simulations, the performance of the controller in combination with the moving horizon estimator is investigated. Based on previous measurements, the MHE adapts the parameters p_i of the polynomial receiver model used by the MPC.

5.3.1 Simulations with Inaccurate Parameter Initialization

In a first step, it is tested if the MHE is able to estimate the parameters of the receiver model correctly. For this, the MPC model is initialized with a set of inaccurate parameters p_i. Each parameter is determined by a random choice following a uniform distribution within the corresponding bounds described in Chapter 4.3.1. The simulations are then performed with and without the MHE using a cloud scenario with a shading of 50 % and an exact prediction $\mathrm{Cloud}_{\mathrm{pred}} = \mathrm{Cloud}_{\mathrm{sim}}$. Figure 5.4 shows the parameters estimated by the MHE during the simulation and the falsely initialized parameters. Additionally, the figure shows the optimal parameters used by the simulator. The system behaviors with and without the use of the MHE are depicted in Figure 5.5. Furthermore, the previous results from Chapter 5.2.1 with the controller and simulator using the same set of model parameters are plotted for reference.

We see that the parameters estimated by the MHE do not match the parameters used by the simulator and change frequently. However, the results of the simulations with the estimated parameters are almost identical to the results with the exact parameters. On the other hand, the performance of the controller with the inaccurate parameter set and without the MHE shows a significant deviation from the reference case without any model uncertainties. The resulting RMSE values for the three depicted cases are listed in Table 5.5.

Table 5.5: RMSE values of T_{out} and $\dot{H}_{\mathrm{out}}$ for different receiver model parameters and a cloud shading of 50 %.

Used parameters	RMSE	
	T_{out}	$\dot{H}_{\mathrm{out}}$
Optimal (fitted) parameters	10.5 K	106.4 kJ s^{-1}
Parameters with uncertainty	18.8 K	433.5 kJ s^{-1}
Parameters adapted by MHE	9.6 K	103.0 kJ s^{-1}

With the use of the MHE an improvement of the RMSE value for the outlet temperature by almost 50 % is obtained, compared to the case with parameter uncertainty. The RMSE value for the enthalpy flow can be reduced by over 75 %, from 433.5 kJ s^{-1} to 103 kJ s^{-1}.

We can conclude that the moving horizon estimator is able to adapt the model parameters to the actual system behavior. This is especially relevant if the original set of parameters is fitted poorly or the system behavior changes over time, for example due to wear of the components.

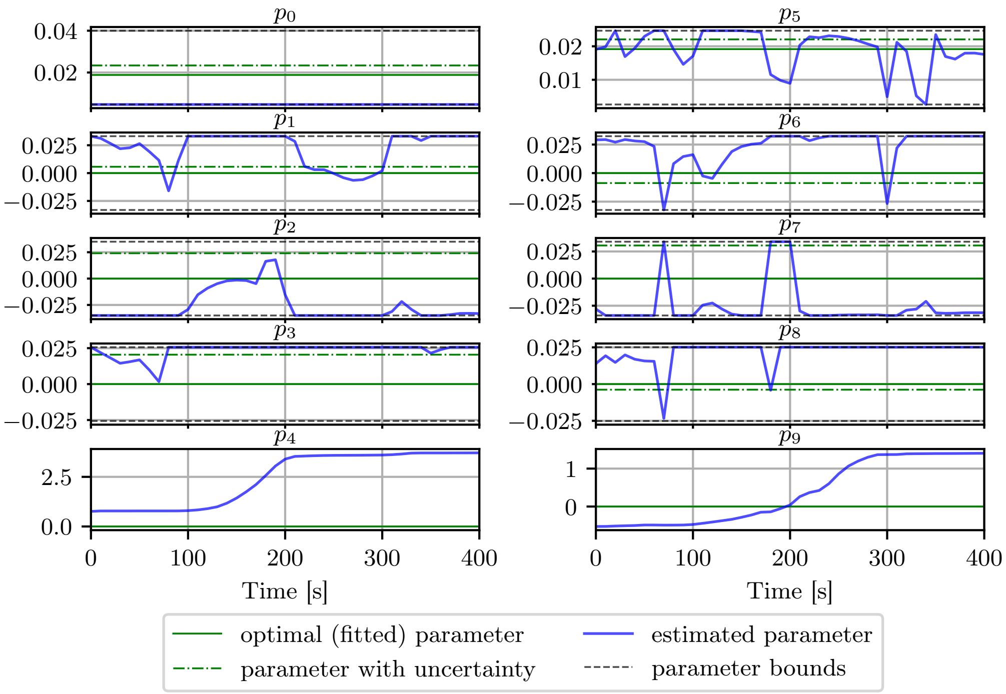

Figure 5.4: Estimated, optimal and uncertain parameters for a shading of 50 %, depicted for Cup 15.

5.3.2 Cloud Scenarios with Inaccurate Cloud Prediction

In a second step, we repeat the simulations with inaccurate cloud predictions from Chapter 5.2.2, now in combination with the MHE parameter estimation. Figure 5.6 shows the simulation results for different cloud predictions. For reference, the previously obtained results without the MHE are depicted as dotted lines.

We see, that for the scenario with the exact prediction of 50 % shading, the results are very similar to the results without the MHE. Thus, the MHE does not affect the control performance negatively for scenarios with accurate cloud predictions. On the other hand, the control performances for the scenarios with inaccurate predictions are improved significantly. For the scenario with the underestimated shading parameter the RMSE values for the outlet temperature and the enthalpy flow are reduced by about 25 % and 20 %, respectively. Even higher improvements can be obtained for the scenario with the overestimated shading parameter, as Table 5.6 shows.

Table 5.6: RMSE values of T_{out} and $\dot{H}_{\text{out}}$ for cloud scenarios with inaccurate shading predictions and use of the MHE in comparison to the control without MHE.

Shading		RMSE		Δ RMSE	
Cloud$_{\text{sim}}$	Cloud$_{\text{pred}}$	T_{out}	$\dot{H}_{\text{out}}$	T_{out}	$\dot{H}_{\text{out}}$
50 %	25 %	27.1 K	248.9 kJ s^{-1}	−24.9 %	−19.5 %
50 %	50 %	9.6 K	102.9 kJ s^{-1}	−8.5 %	−3.3 %
50 %	70 %	6.7 K	125.0 kJ s^{-1}	−59.1 %	−66.6 %

However, in the scenario with a predicted cloud shading of 25 %, an overshooting of

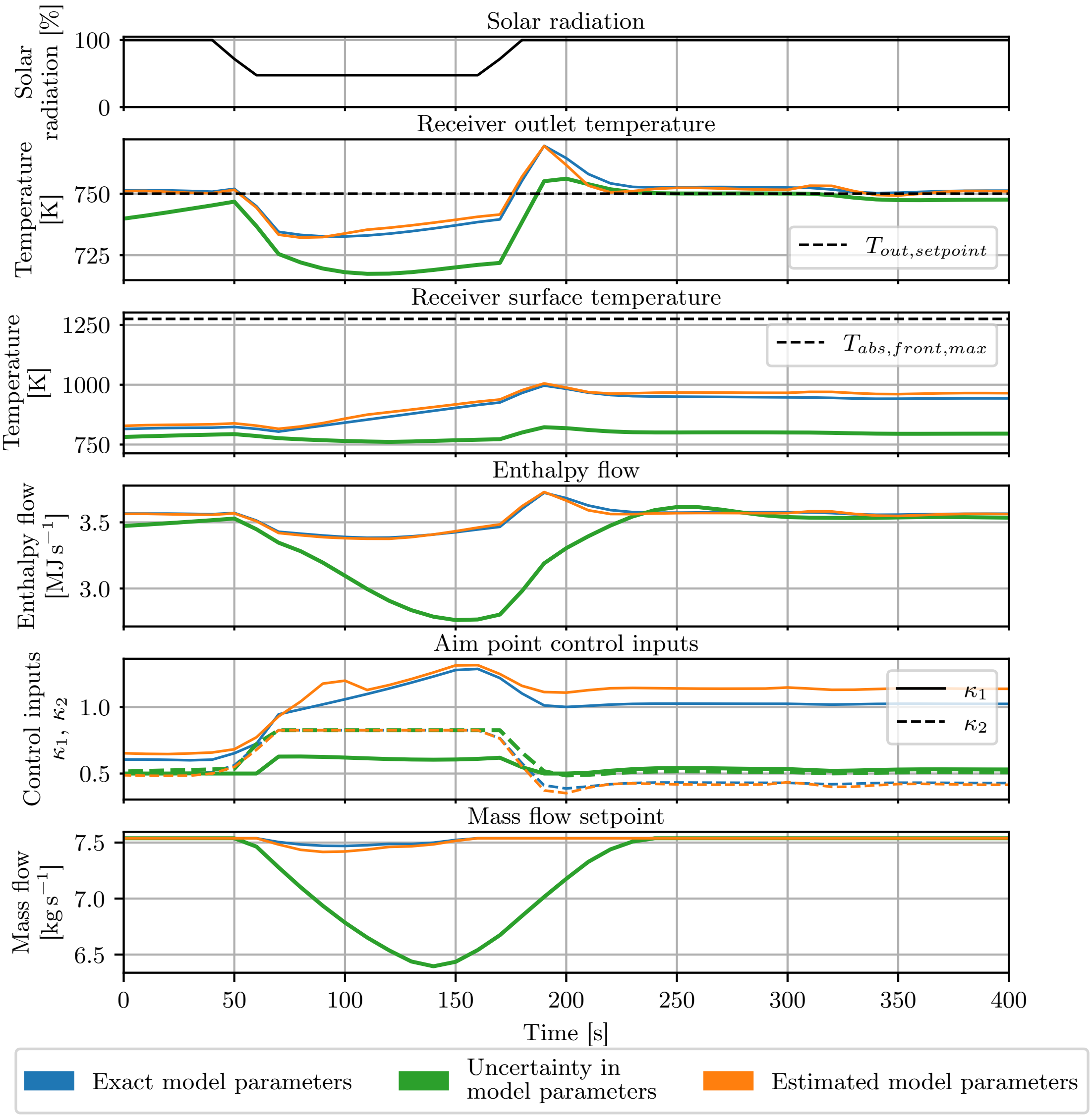

Figure 5.5: System behavior with uncertain parameter initialization with and without MHE and $\text{Cloud}_{\text{pred}} = \text{Cloud}_{\text{sim}} = 50\,\%$.

the outlet temperature can be observed. Thus, even though the RMSE value has been reduced, the maximum range of occurring temperatures remains the same. Similarly, the enthalpy flow rises above its initial value when the cloud passes. A comparable behavior occurs for the scenario with the shading prediction of 70 %. Here, the outlet temperature and enthalpy flow drop when the cloud moves on. These effects are caused by the adapted parameters calculated by the MHE. Figure 5.7 depicts the course of the estimated parameters for the scenario with the shading forecast of 50 %.

We see, that some parameters, like p_5 and p_7, are significantly lower during the cloud passage. The MHE adapts the model behavior to match the current conditions with the available prediction. In this case, it reduces the influence of the solar flux in the model by lowering the parameter p_7, resulting in an overshooting of the temperature when the cloud passes. However, since the overall performance of the control is enhanced, the control design including the MHE will be applied in the experiments.

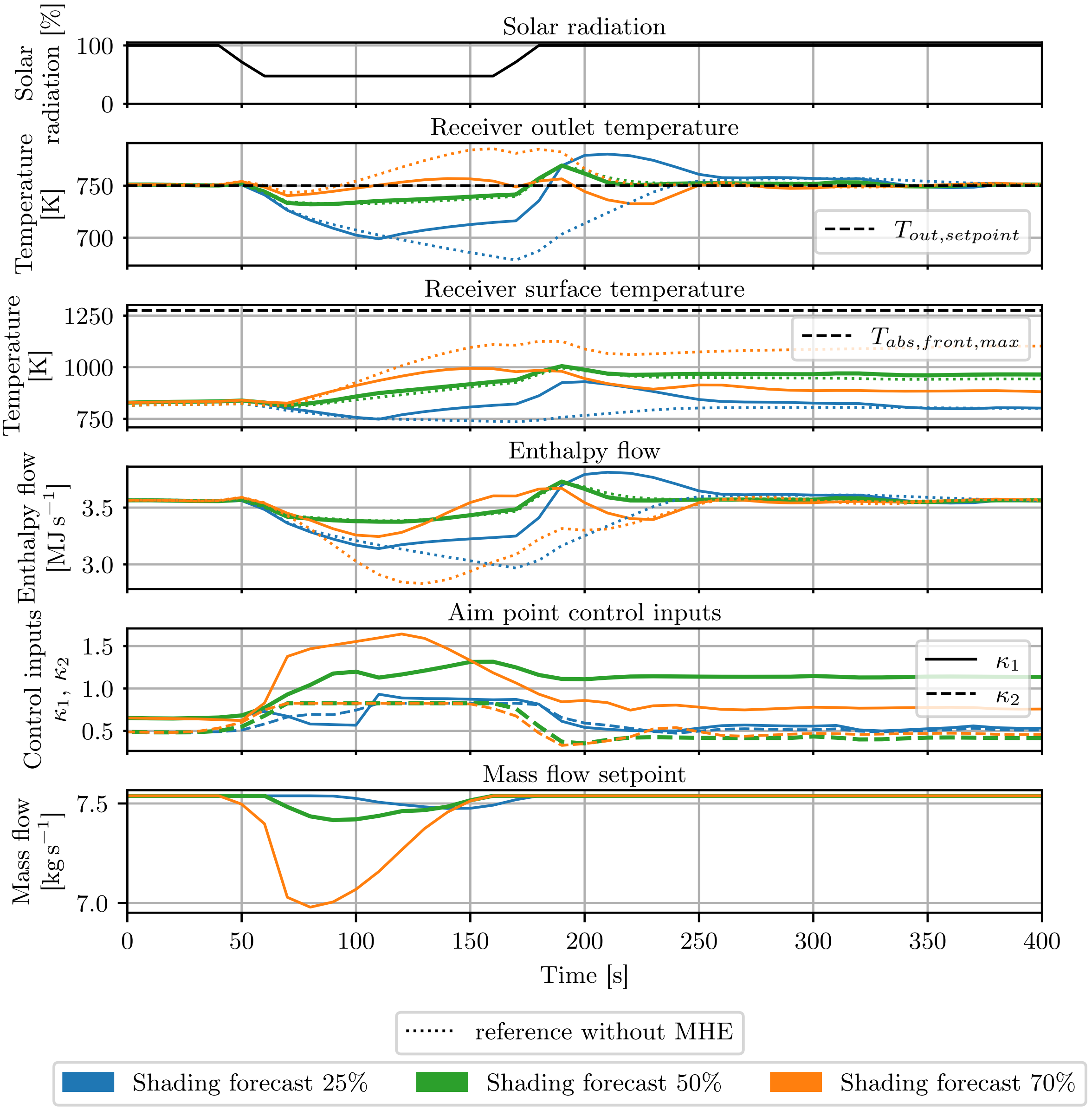

Figure 5.6: System behavior and control actions with MHE for a cloud shading of 50 % and predicted shadings of 25 %, 50 % and 70 %.

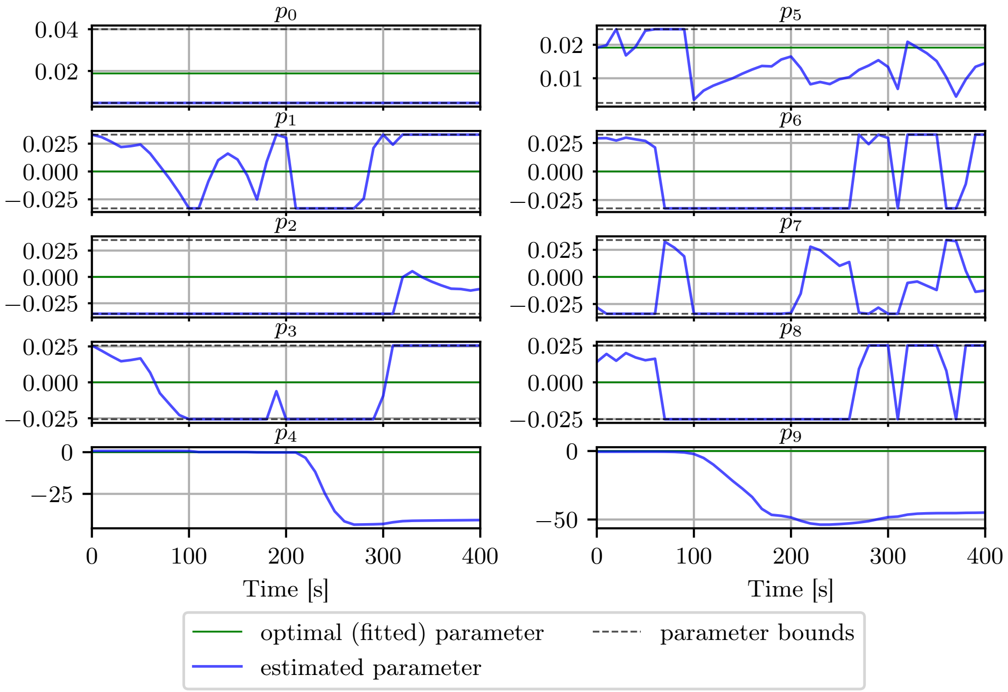

Figure 5.7: Estimated and optimal parameters for a shading of 50 %, depicted for Cup 15.

6 Experiments

In order to evaluate the control performance on the real system, experiments were conducted on the Solar Tower Jülich. The used setup as well as the resulting measurements are presented in this chapter.

6.1 Setup

For the experiments, the Solar Tower Jülich was available for some limited days in September 2023. Since the capacity of the heat storage tank is limited, the steam cycle was activated to dissipate the heat generated in the experiments. In recent years, the tower has not been used in this mode of operation, thus the water steam cycle had to be reactivated specifically for the conduction of the experiments. However, the generated steam was not used for energy conversion in the steam engine. Instead, the steam was redirected through the bypass system and cooled down by the heat exchanger (see Figure 2.1).

The solar flux measurement was not available throughout the experiments. Therefore, the implemented flux density mock-up (see Chapter 4.4), was used to simulate the measured solar flux for each simulated cup.

The experiments were conducted on a similar system than the simulations, differing in the used CPU (Intel(R) Core(TM) i7-10850H @ 2.70 GHz). However, a comparable performance can be expected.

The designed control algorithm was integrated into the solar tower environment as specified in Chapter 4.4. The intention was to assess the control system under various cloud scenarios and different levels of cloud prediction accuracy, in alignment with the simulations conducted in Chapter 5. The cloud scenario definitions can be applied to the heliostat field using the implemented cloud mock-up system. This way, the cloud perturbations are reproducible and thus comparable for different control setups. However, the reproducible execution of the experiments highly depend on stable weather conditions. Ideally, the experiments are conducted during clear-sky conditions.

Unfortunately, the weather conditions in the available time frame were not sufficient to yield reliable results. Additionally, for some experimental runs the parametrization of the MPC has been changed and did not fully align with the parametrization used in the simulations in Chapter 5. Thus, the measurements can only prove the successful setup of the experimental environment and show some preliminary findings.

In the following sections, two measurements from September 28th, 2023 are presented. The day was characterized by a high cloud coverage and thus a low direct normal irradiance. The mean DNI during the measurements was below $300\,\mathrm{W\,m^{-2}}$. For comparison, a clear-sky conditions would yield a DNI value above $700\,\mathrm{W\,m^{-2}}$ at this time of the day.

To account for the low solar irradiance, the set point for the outlet temperature was set to $473\,\mathrm{K}$ for the measurements. The MHE was used in the same setup as described in Chapter 4.3. For the MPC an additional bound on κ_1 was active, restricting its value to $\kappa_1 \leq 1$ instead of the original bound of $\kappa_1 \leq 2.5$. This choice was based on preliminary experiments, where the controller quickly raised κ_2. This caused rapid changes in the receiver temperature, triggering a safety defocus. Note that furthermore the adaption of the weighting factor for κ_1 described in Chapter 5.2.1 was not applied either. Thus, the original value of $w_2 = 3$ was used.

The resulting measurement data is plotted showing the outlet temperature T_{out} and the receiver temperatures $T_{\mathrm{abs,front}}$ and $T_{\mathrm{inlet,3}}$, as well as the control inputs applied to the system. Additionally, the DNI measurement as well as the solar flux from the flux density mock-up are shown. For the solar flux and the surface temperature, only the values of Cup 15 (highlighted in Figure 3.7) are depicted. As in the simulations, a plot of the solar radiation indicates if a simulated cloud has been applied by the cloud mock-up system. The return air temperature $T_{\mathrm{return,3}}$ is not plotted, as it does not show any significant changes throughout the measurement.

For the second presented measurement, the trajectories predicted by the MPC at three different time steps will be included in the plot as well. This way, the implemented model can be compared to the real system behavior.

6.2 Results

6.2.1 Measurement 1: Real Cloud Disturbances without Cloud Prediction

The measurement depicted in Figure 6.1 recorded the system behavior for over 30 minutes, starting at 14:08:32 on September 28th, 2023, local time. The solar radiation plot indicates that no simulated clouds have been applied during the measurement. Instead, the system behavior to the real DNI fluctuations can be observed. Since the experimental setup does not incorporate real-time cloud predictions, the MPC did not have any knowledge about the upcoming DNI changes. Thus, it was limited to react to the incoming DNI measurements but was not able to apply any predictive control actions.

The figure shows that the outlet temperature T_{out} stays close to the set point, yielding an RMSE value of 4.9 K. From the plot of the receiver temperatures, we can observe, that the surface temperature $T_{\mathrm{abs,front}}$ is lower than the outlet temperature $T_{\mathrm{inlet,3}}$ of the corresponding cup. This resonates with the behavior in Chapter 5, where the steady-state was found to be at $T_{\mathrm{abs,front}} < T_{\mathrm{inlet,3}}$ (see Table 5.1). As mentioned before, this is due to the cooling effect of the air flow and the volumetric structure of the receiver. However, since the majority of the solar radiation is absorbed by the absorber cup surface, $T_{\mathrm{abs,front}}$ is effected faster by rising solar flux densities than $T_{\mathrm{inlet,3}}$. This effect is also visible in the plot.

The control inputs applied to the system show, that the bound $\kappa_1 \leq 1$ is very restrictive. The value of κ_1 is mostly changing between its lower and upper bound. Since κ_1 influences how much the aim points are focused on the receiver surface, the changes are visible in the plot of the solar flux density of the central receiver cup as well. Even though the controller is encouraged to minimize the control changes in κ_2, frequent changes in this value can be observed as well. At time 14:33:00 κ_2 even drops to its minimum, defocusing all heliostats. We see that this coincides with the highest DNI value during the measurement.

The mass flow set point, remains close to its minimum value throughout the measurement. As mentioned before, this experiment run uses the weighting factor $w_2 = 3$ instead of the adapted value for the added cost function term J_2. We have seen in the simulations, that this value is too low to effect the enthalpy flow meaningfully and does not lead to a maximization of the mass flow. The measurement confirms this behavior and highlights the importance of the added cost function term and a suitable weighting factor. An increased mass flow could have improved the control performance. With its cooling effect on the outlet temperature, κ_2 could have remained closer to its maximum value to project more solar radiation to the receiver surface. This way, the main control action would have been performed by adapting κ_1.

The last subplot of Figure 6.1 presents the process times of the MHE and MPC. It shows, that the process times in the measurements are significantly higher than in the performance analysis presented in Chapter 4.3.2. With an average time of 3.7 s, the control algorithm takes almost twice as long as in the simulations and exceeds the previously determined limit of 2.1 s. It was found that, despite the comparable CPU specifications, the system used in the simulations overclocked the CPU to a higher frequency. However, this functionality was not enabled on the system used for the experiments. Another contributing factor to the increased process times might be the parallel execution of processes. For example, the communication to the process control system and other remote systems were performed on the same system.

6.2.2 Measurement 2: Simulated and Real Cloud Disturbances

Figure 6.2 shows a measurement conducted on the same day as the first measurement, starting at 12:55:16 local time. Here, a cloud $\text{Cloud}_{\text{sim}}$ with a shading of 25 % was simulated and applied by the cloud mock-up system. The controller was initialized with $\text{Cloud}_{\text{pred}} = \text{Cloud}_{\text{sim}}$. However, the real DNI values during the measurement were again subject to changes with a spread of over $400\,\text{W}\,\text{m}^{-2}$ between the minimum and maximum value. Due to this and the deviating parametrization of the MPC, the analysis of the control performance for the simulated cloud would not yield reliable results. However, the figure also includes additional information about the predictions and calculations made by the MPC. It shows the predicted optimal trajectories for the control inputs as well as the resulting trajectories of the process temperatures and the solar flux. These predictions are plotted for three different time instances and allow an evaluation of the model accuracy implemented in the controller. In each iteration of the MPC algorithm, only the first value of the optimal control input trajectory is applied. Thus, we can only compare the first value of the predicted trajectories to the real system behavior.

We can observe, that for some time instances the predicted trajectories deviate significantly from the measured system behavior. Table 5.5 summarizes and compares the obtained values of $T_{\text{abs,front}}$ and $T_{\text{inlet,3}}$ for the three different time instances.

At the first time instance, the MPC predicts a significant decrease of the receiver temperatures. However, the measured temperature values show an increase. The differences between the predicted and measured values for both receiver temperatures yield approximately 20 K, leading to an overshooting of the outlet temperature.

In the second time instance, the MPC assumes the surface temperature $T_{\text{abs,front}}$ to remain constant in the following time step, whereas $T_{\text{inlet,3}}$ is assumed to rise. The measured data however, shows the exact opposite behavior for the subsequent step: $T_{\text{abs,front}}$ is rising while $T_{\text{inlet,3}}$ is decreasing.

The third time instance on the other hand presents a case where the predicted trajectories for both of the receiver temperatures seem to align with the corresponding measured quantities in the first step. The values in Table 5.5 show that the differences between the predicted and measured values for $T_{\text{abs,front}}$ and $T_{\text{inlet,3}}$ are below 7 K and 7 K, respectively.

Table 6.1: Comparison of the first predicted step to the measured receiver temperatures for three time instances of Measurement 2 (2023/09/28, 12:55:16).

Variable	Timestamp	Measured	Predicted	Difference
$T_{\text{abs,front}}$	15:57:06	593.0 K	569.5 K	−23.5 K
	15:59:06	531.6 K	528.0 K	−3.6 K
	16:11:16	507.5 K	509.4 K	1.9 K
$T_{\text{inlet,3}}$	15:57:06	576.3 K	556.9 K	−19.4 K
	15:59:06	546.4 K	555.0 K	8.6 K
	16:11:16	551.5 K	558.3 K	6.8 K

Figure 6.3 depicts the estimated receiver parameters for Cup 15 for the same measurement. The horizontal lines correspond to the time instances, chosen for the evaluation of the MPC predictions in Figure 6.2. We see that due to the low set point compared to the fitting data, the offset parameters p_8 and p_9 are both estimated to be -150 K or lower. Additionally, the estimated parameters change frequently during the measurement, similar to the results in Chapter 5. It is also noticeable, that the dynamic parameters p_0 and p_4 are at their maximum value at the first highlighted time instance but significantly lower at the other time instances. Since these parameters directly effect the differential equations of the receiver temperatures, their affect is known to be significant for the model behavior. However, since other parameters are changing as well, no clear correlation between specific parameter changes and the differences in the MPC prediction accuracies can be derived.

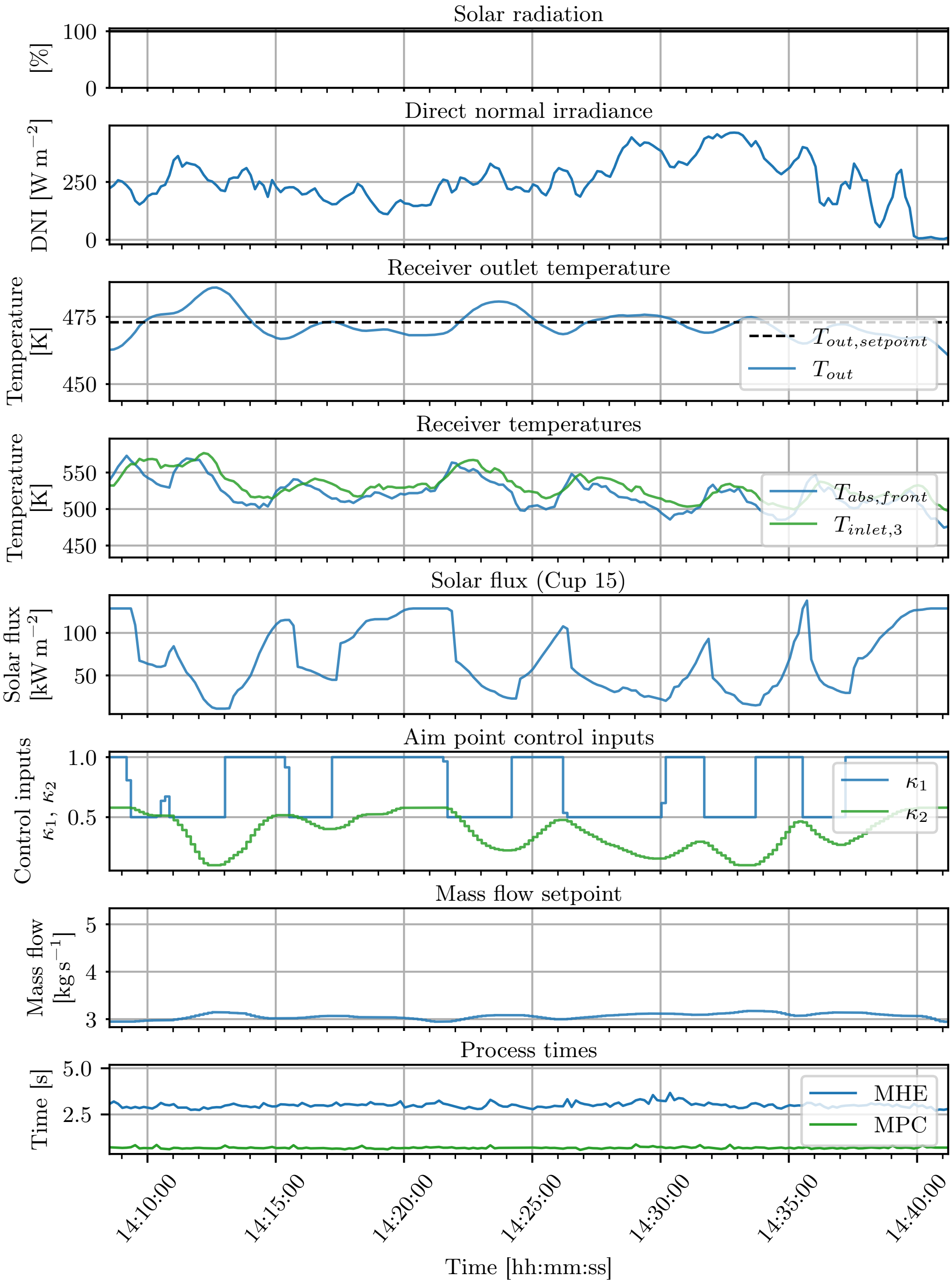

Figure 6.1: Results from Measurement 1 (2023/09/28, 14:08:32).

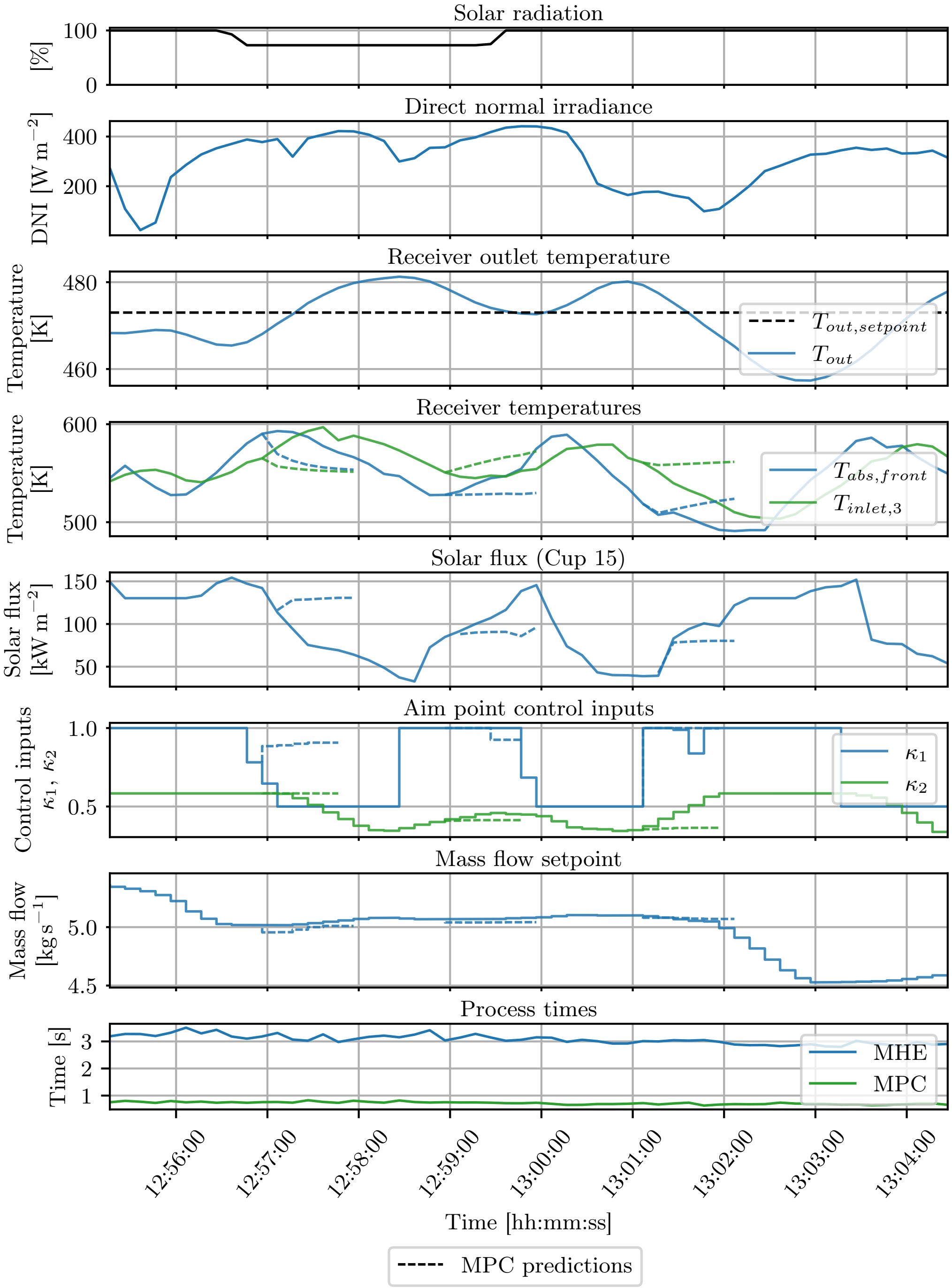

Figure 6.2: Results from Measurement 2 (2023/09/28, 12:55:16), including the predicted trajectories by the MPC.

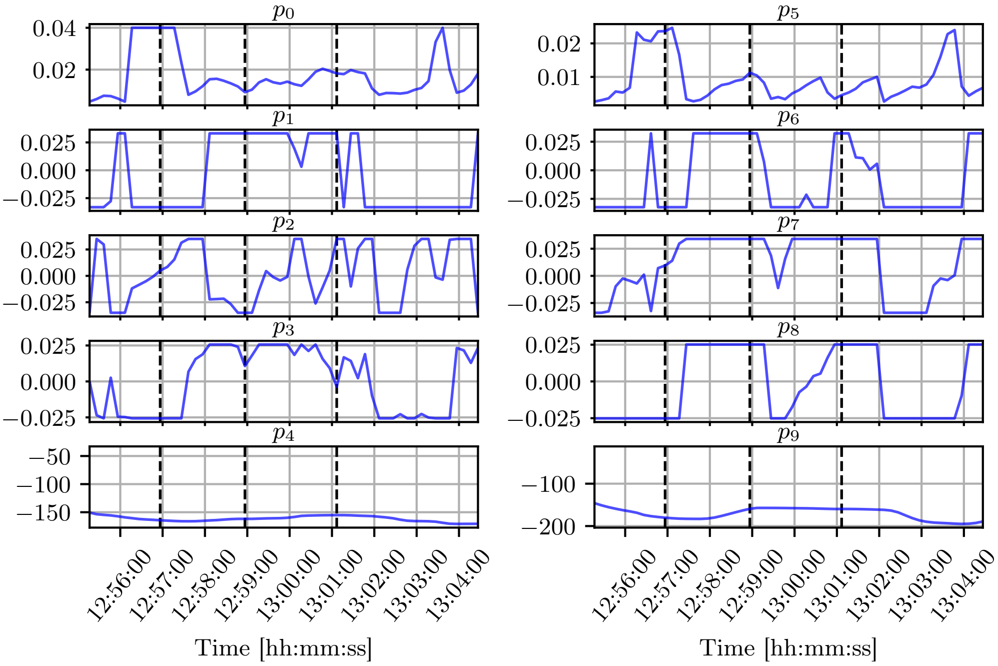

Figure 6.3: Estimated receiver parameters for Measurement 2 (2023/09/28, 12:55:16), depicted for Cup 15.

7 Conclusions and Outlook

In the following, the adaptions on the control design and the results of the simulations and experiments are discussed. Moreover, an outlook on further steps will be given.

Adaptions Due to an enhanced model accuracy, the previously designed model predictive controller by Geschonneck (2023) has been adapted by Zanger (2023) using a polynomial absorber cup model. The model has been calibrated using previously obtained data from the Solar Tower Jülich. The objective function of the controller has been extended to incorporate a metric approximating the enthalpy flow. Additionally, the modified controller now penalizes changes in the time derivatives of the receiver temperatures to prevent a safety defocus triggered by the process control system.

Even though the newly implemented model provided better fitting results, it was assumed that a further enhancement in the model accuracy could be achieved through an additional parameter estimation. Thus, a moving horizon estimator has been designed and implemented in this thesis. It is used to estimate the parameters of the polynomial absorber cup model for each simulated absorber cup individually. This way, the model can be adapted to the current conditions and to operating points that diverge from the fitting data.

Simulations In the simulations, the adaptions on the model predictive control design as well as the improvements by the moving horizon estimator have been investigated. Different cloud scenarios were considered, varying in the shading parameter (relative drop of radiation) and the accuracy of shading parameter prediction.

During the examinations of the new MPC implementation, a further improvement in the weighting factor for the added term of the objective function was found. In contrast to the previous control design, the adaption of the objective function provokes the maximization of the mass flow in order to increase the enthalpy flow of the receiver outlet. This way, the efficiency of the solar tower power plant can be increased. However, the model and the optimization problem do not consider any downstream processes or the energy consumption of the actuators. For example, the addition of a fan efficiency term to the objective function might be beneficial.

The simulations further showed that, as expected, the MPC demonstrates better performance with low shading parameters compared to higher values. Additionally, the control performance was observed to be highly dependent on the accuracy of the cloud prediction. Especially the underestimation of the shading parameters led to a significant deviation of up to 70 K between the receiver outlet temperature and its set point. Furthermore, it was found that due to the multiple aim point control inputs, several optimal solutions for the control problem exist.

The investigations of the extended control design including the MHE, showed that the parameter adaption can improve the model accuracy compared to cases where the fitted model constants are inaccurate. Moreover, the use of the MHE enhanced the performance of the controller for scenarios with inaccurate cloud predictions. The RMSE values of the receiver outlet temperature and the outlet enthalpy flow both reached an improvement of more than 60 % for the overestimated scenario and approximately 20 % for the underestimated scenario.

However, the results also revealed that the MHE does not estimate the parameters to align with the fitted parameters. Instead, the parameters change frequently within the full range of allowed values. The fast adaptions of the model parameters improve the performance of the controller as they adapt the model to the current conditions and the available cloud predictions. Nevertheless, if the conditions and states mostly remain constant within the horizon of the MHE, the adaptions on the model parameters might not fit the dynamic behavior of the system anymore. This can influence the control performance. For example, if a sudden rise in the solar radiation occurs, the MPC might predict the effect on the outlet temperature incorrectly due to the false parameter estimation. Consequently, insufficient control actions are applied by the controller, leading to an overshooting of the outlet temperature. A longer horizon can prevent the MHE from estimating false dynamic parameters as more dynamic events are included in the considered time frame. Similar results about the parameter estimation were observed in the experiments.

Experiments While the experiments could not be conducted as initially planned, the presented measurements still provide a basis for some conclusions.

Firstly, the measurements confirmed the functionality of the experimental setup. Both the cloud mock-up and the flux density mock-up operated as expected.

Moreover, even without prior knowledge of upcoming DNI fluctuations the applied controller kept the receiver outlet temperature close to its set point (RMSE $T_{\mathrm{out}} < 5\,\mathrm{K}$).

However, upon investigating the predicted state trajectories of the MPC, we saw that the adaptions on the model parameters performed by the MHE were not sufficient to align the model to the real plant behavior. Since the MHE has proved to significantly enhance the performance and robustness of the controller in the simulations, it is likely that the implemented model accuracy is not sufficient yet. Thus, even though the polynomial receiver model already achieved better fitting results than the previous physical model, further adaptions on the model will be necessary. With the use of a more extensive set of data, an improvement of the polynomial model fitting might be achievable. However, it is also possible, that the third-order polynomial model is not sufficient to represent the receiver behavior. In this case, a further investigation and improvement of the previous physical model is advisable. If the physical model is found to be more suitable, a state estimation on the unmeasurable state $T_{\mathrm{abs,back}}$ is necessary. Even though not presented in this thesis, an MHE implementation as state estimator for the physical model has been prepared to suit this purpose and can be used for future applications. For both, the polynomial and the physical model, the MHE can also be applied to the measured states. That way, possibly occurring measurement noises can be reduced.

Another important finding from the experiments arose from the measurement of the process times of the MHE and MPC, which exceeded the limit defined in Chapter 4.1 by 1.7 s. Consequently, the real-time capability of the control algorithm is not ensured anymore. However, the process times of the MHE and MPC are still significantly lower than the heliostat movement times. Particularly the delay time before a heliostat reacts to the control input has been found to be the main limiting factor as it averages to 6 s. Thus, an adaption of the update frequency in the heliostat field software HeliOS is the most promising actions to improve the real-time capability of the control. Even though the necessary adaption in HeliOS entails a significant effort, it should be considered in order to enable the implementation of advanced control strategies like the proposed control design.

Summary and outlook In summary, the thesis presented an extension of the MPC control design by a moving horizon estimation. The adapted control has been successfully tested in the simulations. The extension by the MHE yielded better control performances and improved the robustness towards inaccurate cloud predictions. The control design has also been implemented in the environment at the Solar Tower Jülich. However, through the obtained measurement data, several shortcomings of the control design have been revealed. Mainly, the model accuracy of the polynomial absorber cup model has been found to be insufficient to represent the real plant behavior. Moreover, the control loop on the real system is too slow for the applied step time.

Based on the findings, the control design needs further improvements and tests on the real plant. Especially the receiver model should be adapted and validated to ensure sufficient model accuracy.

Before the conduction of further measurements, the experimental setup should be improved as well. Adaptions on either the HeliOS update frequency or the control time step are necessary to ensure real-time capability of the control. Ideally, the complete measurement environment, including the flux density measurement, will be available.

Finally, further experiments on the real plant and in clear-sky conditions should be conducted. With the use of the could mock-up, different cloud scenarios can be simulated to evaluate the performance and robustness of the controller. Further tuning of the weights of the objective function will likely be necessary.

After the control design is improved and tested using the predefined cloud scenarios, it can gradually be tested in more complex scenarios. Eventually, the controller can be connected to the real cloud prediction system and tested in real operation.

Bibliography

Andersson, J. A. E., J. Gillis, G. Horn, et al. (2019). “CasADi: a software framework for nonlinear optimization and optimal control”. In: *Mathematical Programming Computation* 11, pp. 1–36.

Belhomme, B. (2011). “Bewertung und Optimierung von Zielpunktstrategien für solare Turmkraftwerke”. PhD thesis. RWTH Aachen University.

Belhomme, B., R. Pitz-Paal, and P. Schwarzbözl (2014). “Optimization of heliostat aim point selection for central receiver systems based on the ant colony optimization metaheuristic”. In: *Journal of Solar Energy Engineering, Transactions of the ASME* 136.1, p. 011005.

Belhomme, B., R. Pitz-Paal, P. Schwarzbözl, and S. Ulmer (2009). “A New Fast Ray Tracing Tool for High-Precision Simulation of Heliostat Fields”. In: *Journal of Solar Energy Engineering* 131.3, p. 031002.

Boretti, A., S. Castelletto, and S. Al-Zubaidy (2019). “Concentrating solar power tower technology: present status and outlook”. In: *Nonlinear Engineering* 8.1, pp. 10–31.

Capuano, R., T. Fend, P. Schwarzbözl, et al. (2016). “Numerical models of advanced ceramic absorbers for volumetric solar receivers”. In: *Renewable and Sustainable Energy Reviews* 58, pp. 656–665.

Crespi, F., A. Toscani, P. Zani, et al. (2018). “Effect of passing clouds on the dynamic performance of a CSP tower receiver with molten salt heat storage”. In: *Applied Energy* 229, pp. 224–235.

Ding, W. and T. Bauer (2021). “Progress in Research and Development of Molten Chloride Salt Technology for Next Generation Concentrated Solar Power Plants”. In: *Engineering* 7.3, pp. 334–347.

DLR (n.d.). *German Aerospace Center, Solar Towers Jülich.* Accessed: 2023/11/20. URL: `https://www.dlr.de/en/research-and-transfer/research-infrastructure/solar-towers-juelich`.

Gall, J. (2012). “Betriebsführung und-optimierung eines solarthermischen Turmkraftwerkes”. PhD thesis. RWTH Aachen University.

García, J., R. Barraza, Y. C. Soo Too, et al. (2022). “Transient simulation of a control strategy for solar receivers based on mass flow valves adjustments and heliostats aiming”. In: *Renewable Energy* 185, pp. 1221–1244.

García, J., Y. C. Soo Too, R. Vasquez Padilla, et al. (2018). “Multivariable Closed Control Loop Methodology for Heliostat Aiming Manipulation in Solar Central Receiver Systems”. In: *Journal of Solar Energy Engineering* 140.3, p. 031010.

Geschonneck, M. T. (2023). “Modellprädiktive Regelung eines keramischen Receivers für Solartürme”. Bachelor thesis. Technische Hochschule Köln.

Grüne, L. and J. Pannek (2011). *Nonlinear Model Predictive Control: Theory and Algorithms*. Communications and Control Engineering Ser. London: Springer-Verlag London Limited.

Haseltine, E. L. and J. B. Rawlings (2005). “Critical evaluation of extended Kalman filtering and moving-horizon estimation”. In: *Industrial & engineering chemistry research* 44.8, pp. 2451–2460.

Iding, K., D. Zanger, D. Maldanado Quinto, et al. (2023). *A Real-Time Capable Simulation of Open Volumetric Receiver Surface Temperatures with Spatially High Resolution.* Paper presented at 28th SolarPACES Conference 2022.

Julier, S. J. and J. K. Uhlmann (1997). "New extension of the Kalman filter to nonlinear systems". In: *Signal processing, sensor fusion, and target recognition VI.* Vol. 3068. Spie, pp. 182–193.

Lucia, S., A. Tătulea-Codrean, C. Schoppmeyer, et al. (2014). "An environment for the efficient testing and implementation of robust NMPC". In: *2014 IEEE Conference on Control Applications (CCA)*, pp. 1843–1848.

Merchán, R., M. Santos, A. Medina, et al. (2022). "High temperature central tower plants for concentrated solar power: 2021 overview". In: *Renewable and Sustainable Energy Reviews* 155, p. 111828.

do-mpc (2022). *do-mpc python toolbox.* Version 4.4.0.

Nouri, B., S. Wilbert, N. Blum, et al. (2020). "Evaluation of an all sky imager based nowcasting system for distinct conditions and five sites". In: *AIP Conference Proceedings* 2303.1, p. 180006.

Rawlings, J. B., D. Q. Mayne, and M. Diehl (2020). *Model predictive control: theory, computation and design.* 2nd edition. Santa Barbara: Nob Hill Publishing LLC.

REN21 (2023). *Global status report: Energy Supply Module.* Paris: REN21 Secretariat.

Samu, R., S. G. Bhujun, M. Calais, et al. (2022). "Solar Irradiance Nowcasting System Trial and Evaluation for Islanded Microgrid Control Purposes". In: *Energies* 15.17, p. 6100.

Strauß, K. (2009). *Kraftwerkstechnik*. Berlin, Heidelberg: Springer Berlin Heidelberg.

Thonig, R., A. Gilmanova, and J. Lilliestam (2023). *CSP.guru 2023-07-01*.

United Nations (2015). *Adoption of the Paris Agreement.* 21st Conference of the Parties, Paris: United Nations Framework Convention on Climate Change.

Vant-Hull, L. L., M. E. Izygon, and C. L. Pitman (1996). *Real-time computation and control of solar flux density on a central receiver (Solar Two)(protection against excess flux density).* Tech. rep. American Solar Energy Society, Boulder, CO (United States).

Wang, Q.-G. and Z.-Y. Nie (2012). "PID Control for MIMO Processes". In: *PID Control in the Third Millennium: Lessons Learned and New Approaches.* Ed. by R. Vilanova and A. Visioli. London: Springer London, pp. 177–204.

Welch, G. and G. Bishop (2006). "An Introduction to the Kalman Filter". In: *Proc. Siggraph Course* 8.

Zanger, D. (2023). *Personal correspondence.*

Zhang, H. L., J. Baeyens, J. Degrève, et al. (2013). "Concentrated solar power plants: Review and design methodology". In: *Renewable and Sustainable Energy Reviews* 22, pp. 466–481.

Zhu, R. and D. Ni (2023). "A Model Predictive Control Approach for Heliostat Field Power Regulatory Aiming Strategy under Varying Cloud Shadowing Conditions". In: *Energies* 16.7, p. 2997.

A Additional Formulas

A.1 Physical Model of the Absorber Cup

In the following, the physical absorber cup model used in the model predictive control design by Geschonneck (2023) is described. The model is highly simplified using the following assumptions (Iding et al., 2023):

1. Only temperatures are used as state variables.
2. The system is assumed to be isobaric, such that the enthalpy of the air only depends on the temperature.
3. Heat transfer does not occur between neighboring cups, they are assumed to be thermally isolated to each other.
4. The air temperatures are homogeneous within balance spaces and change discretely at balance space boundaries.
5. The absorber comb is the only component with a thermal capacity.

The model is based on the energy balances in different subparts of the absorber cup. The cup is sectioned into the heating zone and the transport zone. The zones and the variables used in the model are displayed in Figure 3.4. In the heating zone, the comb is discretized into the front and back side. Due to the structure of the comb, solar radiation reaches both the front and the back of the comb, which is considered by the factor ξ_{rad}. The solar power can be expressed by the solar flux F_{solar} and the surface of the absorber cup surface A_{abs}:

$$P_{\text{sol}} = A_{\text{abs}} \cdot F_{\text{solar}}. \tag{A.1}$$

The solar radiation absorbed by the front and back side of the comb is then expressed by

$$\dot{Q}_{\text{sol,front}} = \alpha_{\text{sol}} \xi_{\text{rad}} P_{\text{sol}} \tag{A.2}$$

$$\dot{Q}_{\text{sol,back}} = \alpha_{\text{sol}} (1 - \xi_{\text{rad}}) P_{\text{sol}} \tag{A.3}$$

with the solar absorption coefficient α_{sol}.

The change in internal energy of the comb front is given by

$$\dot{U}_{\text{abs,front}} = m_{\text{abs,front}} \cdot c_{\text{abs}} \cdot \frac{\mathrm{d}T_{\text{abs,front}}}{\mathrm{d}t}, \tag{A.4}$$

with the mass of the absorber front $m_{\text{abs,front}}$, the specific heat capacity of the absorber material c_{abs} and the time derivative of the absorber front temperature $T_{\text{abs,front}}$.

Considering the energy balance, another equation can be formulated for $\dot{U}_{\text{abs,front}}$, given by

$$\dot{U}_{\text{abs,front}} = \dot{Q}_{\text{sol,front}} - \dot{Q}_{\text{loss,conv}} - \dot{Q}_{\text{loss,rad}} - \dot{Q}_{\text{comb,front}} - \dot{Q}_{\text{cond}}, \tag{A.5}$$

where $\dot{Q}_{\text{comb,front}}$ denotes the heat exchange between the absorber comb and the incoming air. $\dot{Q}_{\text{cond}}$ represents the conductive heat transfer to the back comb. The loss terms

$\dot{Q}_{\mathrm{loss,conv}}$ and $\dot{Q}_{\mathrm{loss,rad}}$ consider the thermal loss due to wind and radiation, respectively. However, due to its complexity $\dot{Q}_{\mathrm{loss,conv}}$ is not further considered and assumed to be zero. The loss term $\dot{Q}_{\mathrm{loss,rad}}$ is calculated with the Stefan-Boltzmann constant σ, the emission coefficient ϵ and the ambient temperature T_{amb} to

$$\dot{Q}_{\mathrm{loss,rad}} = \epsilon \cdot \sigma \cdot \left(T^4_{\mathrm{abs,front}} - T^4_{\mathrm{amb}}\right). \tag{A.6}$$

With the heat transfer coefficient $\alpha_{\mathrm{comb,front}}$ and the heat transfer surface $A_{\mathrm{comb,front}}$ the heat exchange between the comb and the incoming air is calculated by

$$\begin{aligned} \dot{Q}_{\mathrm{comb,front}} &= \dot{H}_{\mathrm{inlet,1b}} - \dot{H}_{\mathrm{inlet,1}} \\ &= \dot{m}_{\mathrm{abs}} \cdot (h_{\mathrm{inlet,1b}} - h_{\mathrm{inlet,1}}) \\ &= \alpha_{\mathrm{comb,front}} A_{\mathrm{comb,front}} (T_{\mathrm{abs,front}} - T_{\mathrm{m,front}}). \end{aligned} \tag{A.7}$$

The temperature $T_{\mathrm{m,front}}$ is defined as a weighted mean of the inlet temperature $T_{\mathrm{inlet,1}}$ and temperature $T_{\mathrm{inlet,1b}}$ in the midth of the comb. With the weighting factor $w_{\mathrm{T,front}}$ it can be calculated by

$$T_{\mathrm{m,front}} = (1 - w_{\mathrm{T,front}}) T_{\mathrm{inlet,1}} + w_{\mathrm{T,front}} T_{\mathrm{inlet,1b}}. \tag{A.8}$$

From the energy balance in front of the comb, $h_{\mathrm{inlet,1}}$ can be expressed by

$$\dot{H}_{\mathrm{inlet,1}} = arr \cdot \dot{H}_{\mathrm{return,1}} + (1 - arr) \cdot \dot{H}_{\mathrm{amb}} \tag{A.9}$$

where arr denotes the air return ratio. Throughout the whole modeling process, the calculation of the air temperatures based on the specific enthalpy and vice versa is approximated by a third-order polynomial $T = f(h)$ and its inverse $h = f^{-1}(T)$. This is used to achieve a closed representation of the relation between the temperature and enthalpy, reducing the computational cost (Gall, 2012).

Finally, the conductive heat transfer from the front to the back is determined by

$$\dot{Q}_{\mathrm{cond}} = \lambda_{\mathrm{comb}} \cdot \frac{A_{\mathrm{solid}} \cdot (T_{\mathrm{abs,front}} - T_{\mathrm{abs,back}})}{\frac{l_{\mathrm{comb}}}{2}} \tag{A.10}$$

with the thermal conductivity λ_{comb}, the thickness of the comb l_{comb} and the solid absorber front surface A_{solid}.

Similar to the energy balance for the front and assuming the radiation loss is neglectable for the back of the comb, the change in internal energy of the back is approximated by

$$\dot{U}_{\mathrm{abs,back}} = \dot{Q}_{\mathrm{sol,back}} - \dot{Q}_{\mathrm{comb,back}} + \dot{Q}_{\mathrm{cond}}. \tag{A.11}$$

Applying the equivalent steps described in Equations A.4 - A.10 to the back of the comb and combining all stated equations, the differential equations for the absorber front and back can be stated as

$$\begin{aligned} m_{\mathrm{abs,front}} c_{\mathrm{abs}} \frac{\mathrm{d}T_{\mathrm{abs,front}}}{\mathrm{d}t} &= \epsilon \xi_{\mathrm{rad}} A_{\mathrm{abs}} F_{\mathrm{solar}} - \epsilon \sigma A_{\mathrm{abs}} (T^4_{\mathrm{abs,front}} - T^4_{\mathrm{amb}}) \\ &\quad - \alpha_{\mathrm{comb,front}} A_{\mathrm{comb,front}} (T_{\mathrm{abs,front}} - T_{\mathrm{m,front}}) \\ &\quad - \lambda_{\mathrm{comb}} \cdot \frac{A_{\mathrm{solid}} \cdot (T_{\mathrm{abs,front}} - T_{\mathrm{abs,back}})}{l_{\mathrm{comb}/2}} \end{aligned} \tag{A.12}$$

and

$$
\begin{aligned}
m_{\text{abs,back}} c_{\text{abs}} \frac{\mathrm{d}T_{\text{abs,back}}}{\mathrm{d}t} &= \epsilon(1-\xi_{\text{rad}}) A_{\text{abs}} F_{\text{solar}} \\
&- \alpha_{\text{comb,back}} A_{\text{comb,back}} (T_{\text{abs,back}} - T_{\text{m,back}}) \\
&+ \lambda_{\text{comb}} \cdot \frac{A_{\text{solid}} \cdot (T_{\text{abs,front}} - T_{\text{abs,back}})}{l_{\text{comb/2}}}. \qquad (A.13)
\end{aligned}
$$

Finally, the temperatures $T_{\text{inlet,1,b}}$ and $T_{\text{inlet,2}}$ can be derived by the energy balances

$$\dot{Q}_{\text{comb,front}} = \dot{m}_{\text{abs}} \cdot (h_{\text{inlet,1b}} - h_{\text{inlet,1}}) \qquad (A.14)$$

$$\dot{Q}_{\text{comb,back}} = \dot{m}_{\text{abs}} \cdot (h_{\text{inlet,2}} - h_{\text{inlet,}1b}). \qquad (A.15)$$

With $T_{\text{return,3}}$ being a measured variable and thus known, the model is fully described by two differential equations (Equations A.12 - A.13) and two algebraic equations (Equations A.14 - A.15). $T_{\text{abs,front}}$ and $T_{\text{abs,back}}$ serve as state variables and $T_{\text{inlet,1,b}}$ and $T_{\text{inlet,2}}$ as algebraic variables. The outlet temperature of the absorber cup $T_{\text{inlet,3}}$ is then determined by

$$h_{\text{inlet,3}} = h_{\text{inlet,2}} - \frac{\dot{Q}_{\text{loss,i}\to\text{r}}}{\dot{m}_{\text{abs}}} \qquad (A.16)$$

$$T_{\text{inlet,3}} = f(h_{\text{inlet,3}}), \qquad (A.17)$$

considering the heat loss in the transport zone $\dot{Q}_{\text{loss,i}\to\text{r}}$, further described in the following.

Heat Loss in the Transport Zone The heat loss $\dot{Q}_{\text{loss,i}\to\text{r}}$, needed to calculate the outlet temperature of the absorber cup $T_{\text{inlet,3}}$, can be derived by

$$\dot{Q}_{\text{loss,i}\to\text{r}} = C_{\text{i}\to\text{r}} \cdot (T_{\text{inlet,2}} - T_{\text{return,3}}). \qquad (A.18)$$

The used thermal conductance $C_{\text{i}\to\text{r}}$ can be derived using the thermal conductivities of the ceramic λ_{cer}, the insulation λ_{ins} and the pipe λ_{pipe} as well as the local heat transfer coefficients. Additionally, the geometry of the transport zone (see Figure A.1) is needed, leading to

$$
\begin{aligned}
C_{\text{i}\to\text{r}} &= \frac{\pi \cdot l_{\text{B}}}{\frac{1}{\alpha_{\text{inlet,2}} \cdot d_{\text{1,B}}} + \frac{1}{2} \cdot B + \frac{1}{\alpha_{\text{return,3}} \cdot d_{\text{2, B}}}} \\
&+ \frac{\pi \cdot l_{\text{C}}}{\frac{1}{\alpha_{\text{inlet,2}} \cdot d_{\text{1,C}}} + \frac{1}{2} \cdot C + \frac{1}{\alpha_{\text{return,3}} \cdot d_{\text{4,C}}}} \qquad (A.19) \\
&+ \frac{\pi \cdot l_{\text{D}}}{\frac{1}{\alpha_{\text{inlet,2}} \cdot d_{\text{1,D}}} + \frac{1}{2} \cdot D + \frac{1}{\alpha_{\text{return,3}} \cdot d_{\text{3,D}}}}.
\end{aligned}
$$

The coefficients B, C and D are defined as

$$
\begin{aligned}
B &= \frac{1}{\lambda_{\text{cer}}} \cdot \ln \frac{d_{\text{2,B}}}{d_{\text{1,B}}} \\
C &= \frac{1}{\lambda_{\text{ins}}} \cdot \ln \frac{d_{\text{2,C}}}{d_{\text{1,C}}} + \frac{1}{\lambda_{\text{cer}}} \cdot \ln \frac{d_{\text{3,C}}}{d_{\text{2,C}}} + \frac{1}{\lambda_{\text{pipe}}} \cdot \ln \frac{d_{\text{4,C}}}{d_{\text{3,C}}} \qquad (A.20) \\
D &= \frac{1}{\lambda_{\text{ins}}} \cdot \ln \frac{d_{\text{2,D}}}{d_{\text{1,D}}} + \frac{1}{\lambda_{\text{pipe}}} \cdot \ln \frac{d_{\text{3,D}}}{d_{\text{2,D}}}.
\end{aligned}
$$

.

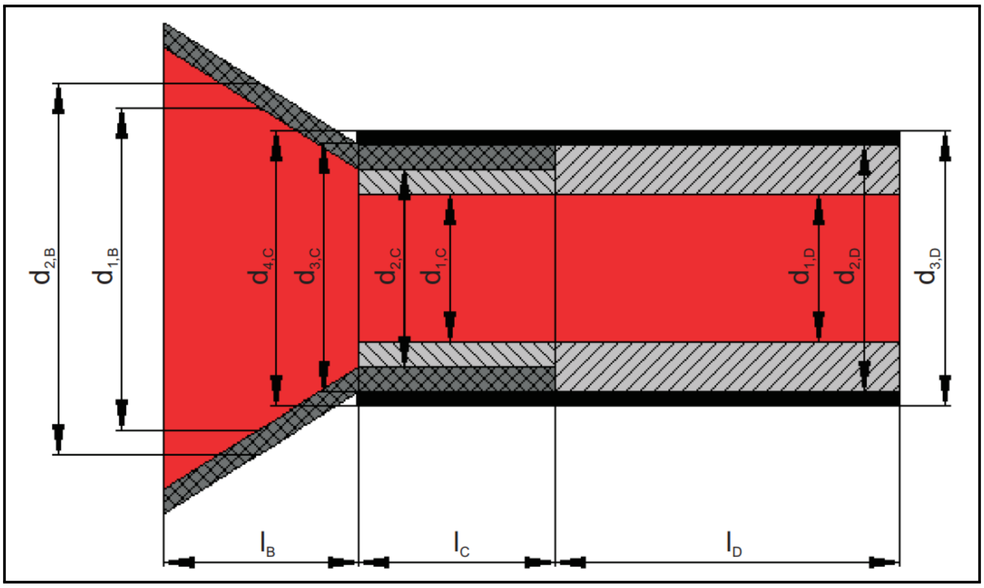

Figure A.1: Geometry of one absorber cup (Gall, 2012).